How a disordered linker in the Polycomb protein Polyhomeotic tunes phase separation and oligomerization

Tim M. Gemeinhardt[1,2,#], Roshan M. Regy[3,#], Andrea J. Mendiola[4], Heather J. Ledterman[4], Amy Henrickson[5], Tien M. Phan[3], Young C. Kim[6], Borries Demeler[5,7], Chongwoo A. Kim[4], Jeetain Mittal[3,8,9,*], Nicole J. Francis[1,2,10,*]

[1]Montreal Clinical Research Institute (IRCM), Montreal, QC, Canada

[2]Division of Experimental Medicine, McGill University, Montreal, QC, Canada

[3]Artie McFerrin Department of Chemical Engineering, Texas A&M University, College Station, TX, USA

[4]Department of Biochemistry and Molecular Genetics, Midwestern University, Glendale, AZ, USA

[5]Department of Chemistry and Biochemistry, The University of Lethbridge, Lethbridge, AB, Canada

[6]Center for Materials Physics and Technology, Naval Research Laboratory, Washington, DC 20375, USA

[7]Department of Chemistry, University of Montana, Missoula, MT, United States

[8]Department of Chemistry, Texas A&M University, College Station, TX, USA

[9]Interdisciplinary Graduate Program in Genetics and Genomics, Texas A&M University, College Station, TX, USA

[10]Department of Biochemistry and Molecular Medicine, University of Montreal, Montreal, QC, Canada

[#]Co-first authors

Summary:

The Polycomb Group (PcG) complex PRC1 represses transcription, forms condensates in cells, and modifies chromatin architecture. These processes are connected through the essential, polymerizing Sterile Alpha Motif (SAM) present in the PRC1 subunit Polyhomeotic (Ph). *In vitro*, Ph SAM drives formation of short oligomers and phase separation with DNA or chromatin in the context of a Ph truncation ("mini-Ph"). Oligomer length is controlled by the long disordered linker (L) that connects the SAM to the rest of Ph--replacing *Drosophila* PhL with the evolutionarily diverged human PHC3L strongly increases oligomerization. How the linker controls SAM polymerization, and how polymerization and the linker affect condensate formation are not know. We analyzed PhL and PHC3L using biochemical assays and molecular dynamics (MD) simulations. PHC3L promotes mini-Ph phase separation and makes it relatively independent of DNA. In MD simulations, basic amino acids in PHC3L form contacts with acidic amino acids in the SAM. Engineering the SAM to make analogous charge-based contacts with PhL increased polymerization and phase separation, partially recapitulating the effects of the PHC3L. Ph to PHC3 linker swaps and SAM surface mutations alter Ph condensate formation in cells, and Ph function in *Drosophila* imaginal discs. Thus, SAM-driven phase separation and polymerization are conserved between flies and mammals, but the underlying mechanisms have diverged through changes to the disordered linker.

Keywords: Sterile Alpha Motif (SAM); Oligomerization; molecular dynamics simulations; phase separation; gene regulation; Polycomb; intrinsically disordered regions (IDRs); biomolecular condensates; analytical ultracentrifugation (AUC); biochemistry

Highlights:

- Disordered linker connecting the SAM to the rest of Polyhomeotic has diverged over evolution
- PHC3L promotes phase separation and changes the underlying mechanism
- PHC3L is predicted to contact the SAM through charge complementary interactions
- Engineered charge complementarity between PhL and SAM promotes oligomerization and phase separation
- Linker interactions modify Ph condensates in cells and Ph function in *Drosophila* imaginal discs

Introduction:

Formation of biomolecular condensates is increasingly recognized as an important mechanism for functional organization of molecules in cells[1], including chromatin and nuclear proteins that regulate its function. Condensates form through multivalent interactions that can involve intrinsically disordered regions (IDRs), oligomerization domains, protein interaction domains, nucleic acid binding domains, or combinations of these[2,4,6]. The physical properties and dynamics of condensates span broad ranges and can change over time or in response to conditions[1,6]. The full range of condensate properties in cells are just beginning to be elucidated. Determining the mechanism of condensate formation and their physical properties is essential to understanding their function.

Gene regulation involves regulation of chromatin, ranging from histone post-translational modifications to large-scale organization[8,10,12,14,16]. Condensate formation is implicated in many aspects of gene regulation. This includes epigenetic regulation by the Polycomb group (PcG) proteins, which govern gene expression patterns through their influence on chromatin structure[18,20,22,24,26]. Two major PcG complexes, PRC1 and PRC2, catalyze the deposition of specific histone modifications, H3K27me3 and H2AK119ub, respectively. PcG proteins also regulate chromatin architecture, from local compaction to the formation of large-scale domains. PcG proteins form condensates (or "bodies") in nuclei[28,30,32,34,36,38], that colocalize with repressed genes [32,40,42,44,46]. Unlike transcription activation, which is a rapid process and involves dynamic condensates[48], PcG regulation can be stable and heritable. One hypothesis is that stable condensates with slow dynamics are used for long-lived processes like molecular memory while more dynamic ones are used for processes under rapid regulation (like transcription activation).

While both PRC1 and PRC2 localize to PcG condensates, PRC1 is more implicated in their formation and in both long- and short-range chromatin organization[32,34,44,50,52,54]. PRC1 consists of 4 subunits in *Drosophila* (human homologs in brackets): Ph (PHC), Pc (CBX), Psc (PCGF), and dRING (RNF2). Of these four, Pc and Ph are most implicated in regulating chromatin architecture[34,44,46,56]. Regulation of chromatin architecture by Ph/PHCs depends on a conserved

oligomerization domain called the Sterile Alpha Motif (SAM)[18,40,42,58]. Ph SAM forms helical polymers *in vitro*, which depend on a head to tail interface formed by end helix, and mid loop (ML). Disrupting this interface disrupts PcG clustering and gene regulation[32,34]. However, Ph lacking the SAM cannot rescue any *ph* functions, while *ph* with the polymerization interface mutated rescues some but not all functions[42]. This indicates that Ph SAM has essential activity in gene regulation beyond oligomerization. The ability of CBX proteins to drive phase separation of mammalian PRC1 and chromatin has also been investigated[60,62]. An IDR in CBX2 undergoes phase separation *in vitro*[36,60,64], and Cbx2 forms condensates with properties consistent with phase separation *in vivo*[60,62,66] and is implicated in chromatin architecture and gene regulation *in vivo*[68,70]. PHC and CBX activities must be coordinated in PRC1, and recent work indicates a prominent role for Cbx2 in controlling mammalian PRC1 condensates[64]. In *Drosophila* embryos, Ph condensates form in mutants lacking Pc, while Pc condensates do not form in mutants lacking Ph[44]. Thus, in *Drosophila*, Ph may be more central to PcG condensates than Pc. We are therefore dissecting Ph function as a means to understand condensate formation and chromatin organization.

Ph is a large protein (1589 aa), that has ~1200 amino acids of low complexity sequence that is predicted to be disordered in its N-terminal region[72], followed by a domain termed HD1 that is required for assembly into PRC1[73], and an FCS Zn finger that can bind DNA and RNA[74]. These domains are separated from the SAM by a long (>100 aa) disordered linker. A truncated Ph containing the HD1, FCS, linker and SAM ("mini-Ph") can undergo phase separation with DNA or chromatin[75], and this activity depends on the SAM. Mini-Ph with the EH or ML SAM polymerization interfaces mutated requires higher protein concentrations for phase separation. The condensates formed by mutant mini-Ph are dissolved at lower salt than those formed by wild-type protein, and mutant mini-Ph has both a higher mobile fraction and faster recovery in FRAP assays[75]. Thus, phase separation depends on Ph SAM, and is enhanced by but does not require oligomerization activity.

In mammals, Ph has three homologues, PHC1-3. The basic domain architecture of Ph and the sequence and structure of the SAM are well-conserved. However, within the mini-Ph region, the linker connecting the SAM to the FCS is diverged, and this has functional consequences for SAM oligomerization. While Ph SAM forms open-ended polymers *in vitro*, attaching the Ph linker (PhL) restricts polymerization to ~4-6 units[18]. In contrast, the human PHC3 linker (PHC3L) enhances rather than restricts oligomerization[18]. The comparison of PhL and PHC3L is thus a natural experiment to dissect mechanisms of oligomerization control, condensate formation, and the interplay between the two.

Here, we swapped PhL with PHC3L in *Drosophila* (mini-)Ph and found that PHC3L increases phase separation propensity and alters both the properties of the condensates that form and the requirements. We developed a mechanistic model for linker control of phase separation and oligomerization that is based on molecular dynamics (MD) simulations and supported by *in vitro* and *in vivo* experiments.

Results

The linker sequence changes phase separation propensity and condensate properties. We previously found that disrupting SAM polymerization decreases the propensity of mini-Ph to phase separate with DNA. To determine how increasing SAM polymerization affects condensates, we created *Drosophila*-human chimeric proteins in which the Ph linker (PhL) (polymerization limiting) is replaced by that of PHC3 linker (PHC3L) (polymerization promoting) in mini-Ph (**Fig. 1A**). Use of chimeric proteins makes it possible to isolate effects of the linker from other sequence changes between Ph and PHC3. We tested phase separation of mini-Ph and mini-Ph-PHC3L with DNA and found that mini-Ph-PHC3L phase separates at ~8x lower concentration than mini-Ph (**Fig. 1B,C**). At equivalent protein concentrations, the condensates formed with mini-Ph-PHC3L are smaller than mini-Ph condensates, and remain small after overnight incubation (**Fig. 1D,F**). mini-Ph condensates progressively fuse and wet the untreated glass surface at all concentrations where condensates are observed, but higher concentrations of PHC3L are required for wetting and fusion even after overnight incubation (**Fig. 1E,G**).

mini-Ph does not phase separate in the absence of DNA or crowding reagents[75]. In contrast, mini-Ph-PHC3L undergoes phase separation as soon as the salt concentration is lowered, without a requirement for DNA (**Fig. 1B**). Titrations indicate that DNA does not have a strong effect on the phase boundary of mini-Ph-PHC3L (unlike mini-Ph) (**Fig. 1C**), or on condensate size (**Fig. 1H**) or wetting/fusion behavior (**Fig. 1I**). Indeed, mini-Ph-PHC3L forms condensates at slightly lower concentrations in the absence of DNA (**Fig. 1C**). mini-Ph lacking the FCS zinc finger, which can bind nucleic acids[74], and the HD1, does not phase separate with DNA in vitro[75]. Since mini-Ph PHC3L phase separates without DNA, we wondered if the FCS and HD1 are still required. We produced linker-SAM proteins (i.e., mini-Ph ΔHD1/FCS with PhL and PHC3L) in *E. coli* using the cleavable SUMO solubility tag. As expected, upon lowering the salt concentration PhL-SAM does not form condensates, either before or after SUMO cleavage by Ulp1 (**Sup. Fig. 1E, Fig. 1J)**. In contrast, PHC3L-SAM forms condensates both before (**Sup. Fig. 1E)** and after Ulp1 cleavage (**Fig. 1J**). Condensates formed with the intact SUMO tag are large and round, while those formed after cleavage are small and irregularly shaped. Taken together, these results demonstrate that the PHC3L lowers the threshold for phase separation, changes the nature of the condensates that form, and changes the underlying mechanism since the HD1, FCS domains and DNA are not required.

MD simulations predict PHC3 but not Ph linker to interact with the SAM, and with itself. To identify interactions involving linker and SAM that could regulate polymerization, phase separation, or both, and explain the distinct mechanisms for phase separation with PhL versus PHC3L, we carried out MD simulations. We used a recently developed coarse-grained (CG) model, the Hydropathy Scale (HPS) – Urry model (see Methods), which has been shown to have good agreement with the experimentally observed phase behavior of a diverse set of IDP sequences and multidomain proteins such as HP1α[76,77]. CG simulations of a single molecule of PhL or PHC3L attached to the Ph SAM domain were conducted (a snapshot of a linker-SAM construct is shown in **Fig. 2A**). From these single chain simulations, we calculated the average intramolecular

contacts formed between the linker and the SAM domain to quantify interactions of PhL and PHC3L with SAM, which are shown in the form of heatmaps (**Fig. 2B, C**).

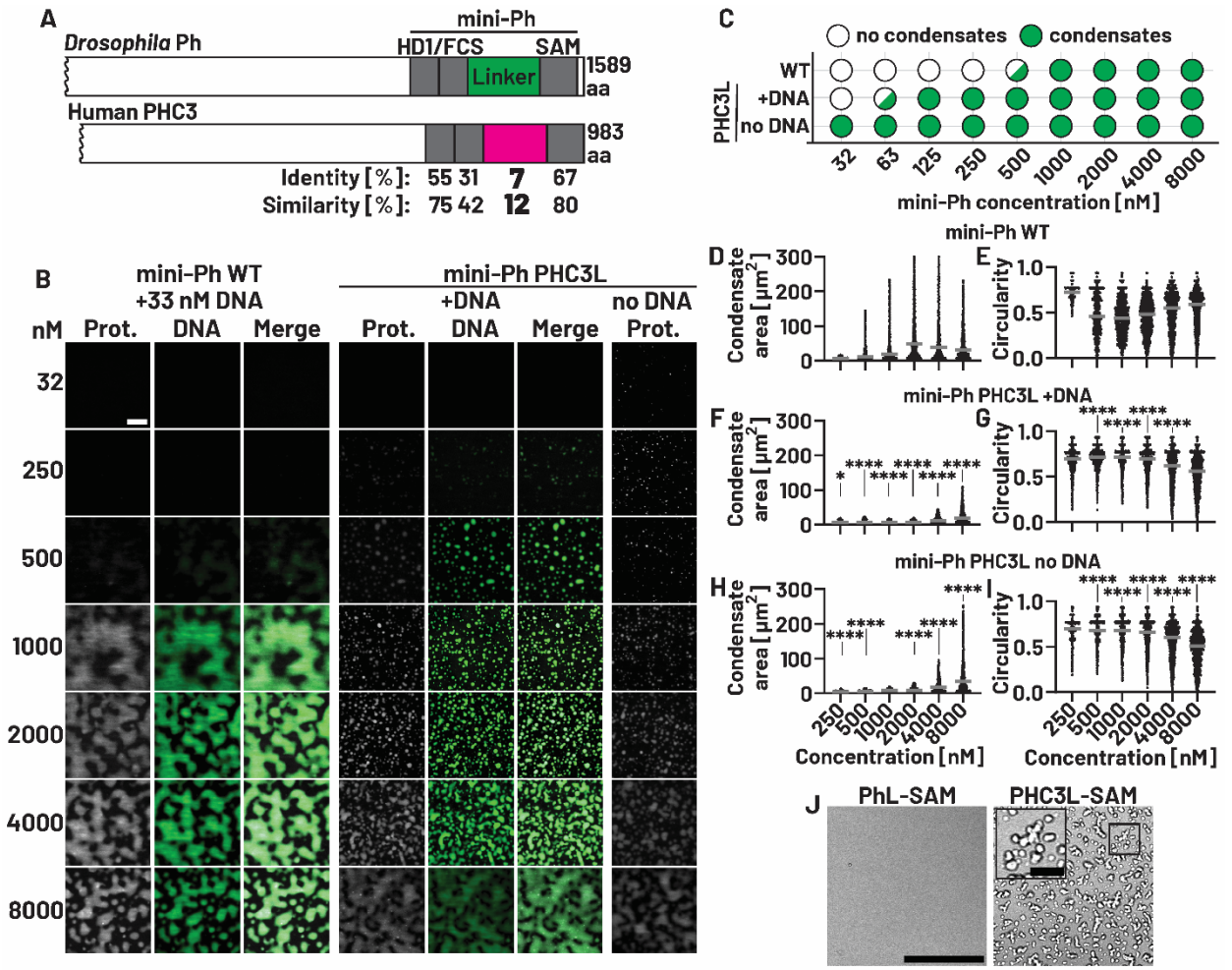

Figure 1: Effect of linker sequence on phase separation of mini-Ph *in vitro*. A. Schematics of *Drosophila melanogaster* Ph and human PHC3. B. Images from mini-Ph WT or mini-Ph PHC3L titrations after overnight incubation. Proteins were labelled with Cy3 and DNA (33 nM, 156 bp dsDNA) was visualized with YOYO1. Scale bar: 20 µm. C. Summary of titration experiments demonstrating that mini-Ph PHC3L with or without DNA forms condensates at lower concentrations than mini-Ph. D-I. Quantification of area and circularity of condensates from three experiments. Grey bars indicate median values. Data were compared using Dunn's test for multiple comparison (*: $p<0.05$, ****: $p<0.0001$). Indicated comparisons were WT vs. PHC3L with DNA (i.e. D vs. F, E vs. G) and PHC3L with DNA vs. PHC3L without DNA (i.e. F vs. H, G vs. I), respectively. J. Phase contrast images of PhL-SAM (mini-Ph ΔHD1/FCS) and PHC3L-SAM upon cleavage of SUMO tag with Ulp1. Scale bar: 50 µm and 10 µm for inlay. All phase separation assays were conducted at 60mM KCl.

Comparing both contact maps, we observe that multiple segments of the PHC3L interact with the SAM, whereas the PhL only has noticeable local interactions near the SAM attachment site. PHC3L is basic (pI=11) and has a high Fraction of Charged Residues (FCR 34%, net charge +5), while the PhL is acidic (pI=4) and has a lower fraction of charged residues (FCR 15%, net charge -7) (**Fig. 2D,E**)[75]. Contacts in the simulations involve, among others, charged residues—specifically, R and K residues in PHC3L frequently interact with D and E residues on the SAM (**Sup. Fig. 2B**). Two prominent patches on the SAM feature conserved acidic residues in tandem, namely Ph residues D1516/D1517 (referred to as "16/17") and residues D1533/D1534 (referred to as "33/34") (**Sup. Fig. 2A**). Strong interactions are observed between these patches and the N-terminal region of the PHC3L.

To determine whether linker-SAM interactions can capture the changes in phase separation observed with mini-Ph with different linkers, we conducted multichain MD simulations of the two linker–SAM constructs. Simulations were conducted at 300 K and 100 mM salt concentration. Exemplary simulation frames are shown in **Fig. 2F** and **G**. Densities of the coexisting dense and dilute phases were calculated from these simulations. PHC3L-SAM shows higher phase separation propensity (nearly two orders of magnitude lower c_{sat}) than PhL-SAM (**Fig. 2H**), which is qualitatively consistent with *in vitro* phase separation assays of PhL-SAM and PHC3L-SAM (**Fig. 1**). In addition to heterotypic interactions between linker and SAM, homotypic linker interactions could contribute to the observed phase separation behavior. To estimate the contribution of linker-linker interactions to phase separation, we calculated the radius of gyration (R_g) and intrachain distances for each linker sequence from single chain simulations (**Fig. 2I**). Both metrics provide complementary information on the single chain conformational properties, which have been shown to have a good correlation with phase separation propensity for natural sequences[78]. We calculated the average interresidue distance R_{ij} between the i^{th} and j^{th} residue as a function of residue separation, $|i-j|$. We then fit the distribution of interresidue distances to the power law $R_{ij} = b|i-j|^{\nu}$ where b is the Kuhn length, which is set to 0.55 for disordered proteins and ν is the polymer scaling exponent. An ν value equal to 0.33 or below indicates that the polymer is in a collapsed or globular conformation. If ν is equal to 0.5 then the polymer acts as an ideal chain and if ν is close to 0.588 then the polymer acts as an expanded chain. As shown in **Fig. 2I**, PhL lies between the expanded and ideal chain regimes, but it is quite close to behaving like an ideal chain. All human homologs on the other hand are more collapsed and lie between the ideal chain and the globular chain limit. The R_g behaves similarly, where PhL is the most expanded chain and PHC3L is most collapsed. Consistent with these observations, we observe more frequent non-local intramolecular contacts in the case of PHC3L (**Fig. 2K**) as compared to PhL (**Fig. 2J**) in single chain simulations.

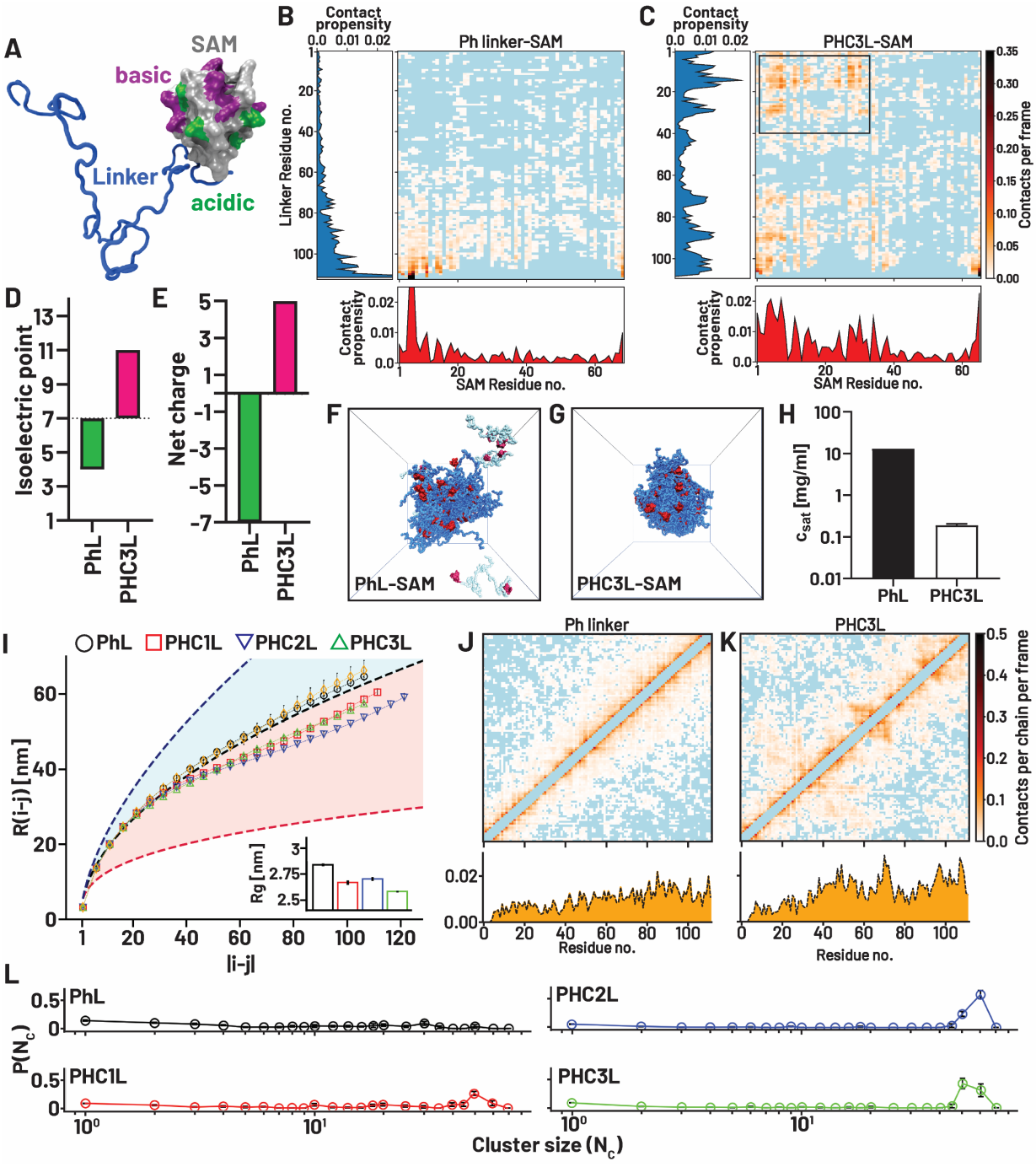

Figure 2: Molecular Dynamics simulations of Ph linker and PHC3L with SAM, and alone. A. Snapshot of linker-SAM model used for simulations. The SAM (PDB 1KW4) is simulated as a rigid body; basic and acidic patches on the SAM are highlighted. B, C. Contact maps from single chain simulations show contact frequencies between linker residues and SAM residues (non-interacting residues colored in light blue) for PhL-SAM (B), and PHC3L-SAM (C). D. The isoelectric point of the linker distinguishes the acidic PhL from the basic PHC3L. E. PHC3L is more positively charged than the PhL. F, G. Snapshots from multichain simulations of PhL-SAM (F) and PHC3L-SAM (G). SAM is red, and linkers are blue. Linkers that are not part of the largest cluster are colored light blue. H. Computed saturation concentration from multi chain simulation is lower for PHC3L-SAM than for PhL-SAM chains. I. Intrachain distance distributions (i.e. distribution of distances between ith and jth residue on the linker sequence) and radius of gyration (inset) calculated from single chain simulations show PHC1-3L with higher compaction compared to PhL. Blue dashed line represents the expanded chain limit, black dashed line represents the ideal chain limit and the red dashed line represents the collapsed or globular chain limit. J, K. Intramolecular interactions from single chain simulations of PhL (J) and PHC3L (K) show increased interactions in the latter. A diagonal band of contacts between 3 neighboring residues is removed from the plot to highlight long range contacts. L. Linkers do not phase separate avidly in simulations, but higher clustering is observed for PHCLs compared to PhL.

To compare the propensity of linker sequences to phase separate, we also conducted multichain simulations with each of the three PHC linkers and PhL. All linker sequences showed weak tendency to form phase separated droplets, and instead formed few dispersed clusters that varied in size (**Sup. Fig. 2C**). Even upon increasing the solution concentration further by reducing the simulation box size, we did not observe the formation of a distinct condensed phase indicating that homotypic linker interactions are not sufficient to explain mini-Ph or mini-Ph-PHC3L phase separation. Nevertheless, we compared the self-assembly of each linker by calculating the distribution of cluster sizes from the multichain simulations (**Fig. 2L, Sup. Fig. 2C**). Single chain collapse and cluster sizes are correlated, with both increasing for human linkers, particularly PHC2 and PHC3 linkers. We infer that human homologs of the linker sequence have higher homotypic interactions than their fly counterpart.

Taken together, MD simulations indicate that linker-SAM and linker-linker contacts differentiate PhL from PHCLs. These contacts, especially linker-SAM contacts, are driven by charged residues, and are predicted to drive the increased phase separation propensity of mini-Ph PHC3L (and PHC3L-SAM) compared to mini-Ph (and PhL-SAM) in agreement with our experimental data (**Fig. 1**).

A charge complementarity model can explain effects of PHC3L on SAM oligomerization and phase separation *in silico*. The simulations suggest that charge-based interactions between PHC3L and SAM could explain its effects on polymerization and phase separation. To test this hypothesis, we designed mutations on the surface of the SAM that could make charge-based interactions with the PhL. Specifically, the two pairs of tandem aspartic acid (D) residues that interact with PHC3L were mutated to arginine (R) and lysine (K) ("D16K/D17R" and "D33K/D34R"). This switches small negative patches to positive, to potentially drive interactions with negatively charged residues in PhL. The negative patches are conserved in PHC3 SAM, although the D34 position is an E in PHC3 (**Sup. Fig. 2A**). The net charge of the SAM is -4; mutation of a single acidic patch neutralizes the SAM net charge and mutation of both patches inverts it to +4 (combined mutations of D16K/D17R and D33K/D34R are referred to as SAMsurf) (**Fig. 3A**).

To determine the effects of the SAM surface mutations on SAM-SAM interactions, we conducted multichain simulations of the SAM. While our CG model does not fully capture canonical SAM oligomerization, we observed non-canonical clustering of WT SAM chains (**Fig. 3B, Sup. Fig. 3A**). Neutralizing the SAM charge by introducing single pairs of mutations resulted in an increased clustering of SAM chains, which may be a result of reduced electrostatic repulsion. Importantly, introduction of both pairs of mutations abolished SAM clustering completely. These data suggest that non-canonical SAM binding may contribute to protein assembly and phase separation *in silico* and possibly in experiments. In addition to linker-SAM contacts, SAM clustering may explain enhanced phase separation of linker-SAM chains vs linker chains (**Fig. 2F+G, Sup. Fig. 2C**). Attaching the SAM switches the poorly clustered PhL to a fuzzy droplet-like cluster in coexistence with protein chains in the dilute phase, and the system-wide cluster of PHC3L chains to a distinct droplet with very few proteins in the dilute phase. We previously found that mini-Ph that cannot polymerize due to mutation of the polymerization interface can phase separate with DNA or chromatin, while mini-Ph lacking the SAM cannot[75]. This indicated that SAM makes additional undescribed interactions; non-canonical interactions that mediate SAM-SAM clustering may explain this result.

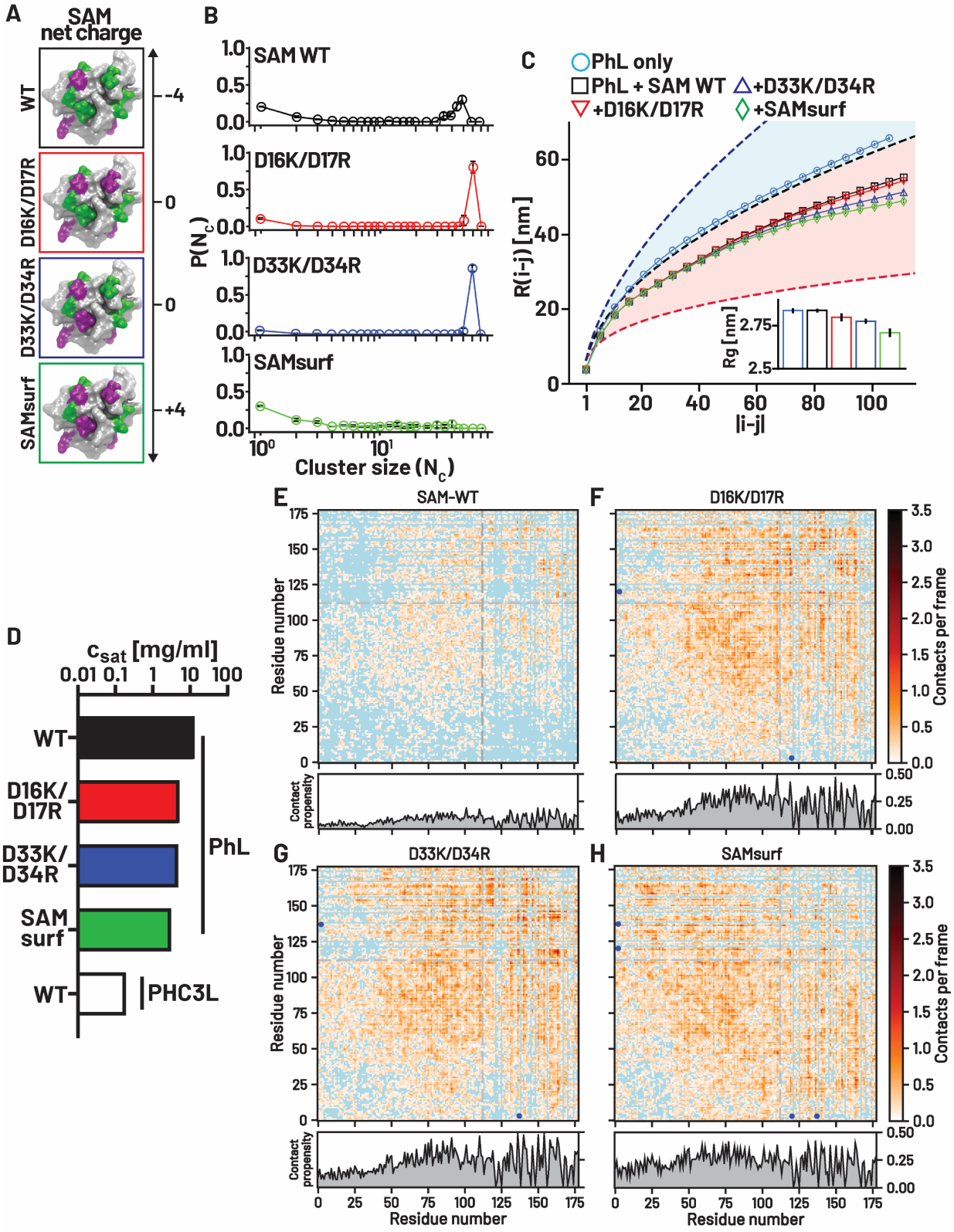

Figure 3: Molecular Dynamics simulations of Ph linker with SAM surface charge mutants. A. SAM mutants were designed to change acidic residues (green) on the SAM surface to basic ones (magenta). B. SAM WT forms some clusters in simulations, which are increased for D16K D17R and D33K D34R but abolished when both pairs of surface mutations are introduced (D16K D17R D33K D34R, "SAMsurf"). C. Intrachain distance distributions (i.e. distribution of distances between ith and jth residue on the linker sequence) and radius of gyration (inset) calculated from single chain simulations show PhL with SAM surface charge mutants have a higher compaction compared to PhL with WT SAM. Blue dashed line represents the expanded chain limit, black dashed line represents the ideal chain limit and the red dashed line represents the collapsed or globular chain limit. D. Computed saturation concentrations from multichain simulation is lowest for PHC3L-WT SAM, intermediate for PhL-SAM surface charge mutants and highest for PhL-WT SAM chains. E-H. Intermolecular contact maps from multi chain simulations of PhL with WT SAM (E), D16K/D17R SAM (F), D33K/D34R (G) and SAMsurf (H) show overall contact frequencies increase for PhL with SAM surface charge mutants compared to WT SAM (non-interacting residues colored in blue). Grey lines mark linker-SAM boundary; blue dots indicate mutated sites.

To dissect how the SAM surface mutations affect interactions with linkers, we first conducted single chain simulations. We measured the impact of each SAM mutant on the polymer scaling and R_g of PhL. We observe further linker collapse as the overall SAM charge increases (**Fig. 3C** and inset). We also observe increasing linker-SAM interactions in intermolecular contact maps from multichain simulations, which correlate with increases in the overall SAM charge (**Fig. 3E-H, Sup. Fig. 3B**). As expected, amino acids involved in contacts include acidic residues in PhL, and the basic patches on the SAM (**Sup. Fig 3C**). This suggests that the overall charge complementarity of SAM and linker introduces PhL-SAM interactions.

Multichain simulations of PhL with SAM surface mutants predict a small increase in phase separation propensity (lower c_{sat}) relative to WT (**Fig. 3D**), although c_{sat} is still higher than for PHC3L-SAM (**Fig. 3D**). This gap may be explained by the additional contribution to phase separation through the linker-linker interactions of PHC3L, and loss of SAM-SAM clustering in the case of the 4-residue mutant, SAMsurf (**Fig. 3B**). Taken together, simulations confirm new PhL-SAM interactions occur upon introducing basic patches to SAM. Our data suggest a charge complementarity model can explain linker-SAM interactions in simulations.

Introducing charge complementarity between PhL and SAM promotes SAM oligomerization. To test the importance of linker-SAM contacts driven by charge complementarity for SAM oligomerization, we used Analytical Ultra Centrifugation (AUC). We previously used sedimentation velocity analytical ultra centrifugation (SV-AUC) extensively to analyze SAM polymerization, including the effects of PhL and PHC3L[18]. We measured the corrected sedimentation coefficients alongside their corresponding boundary segments for PhL attached to different SAMs (**Fig. 4A**). For WT PhL-SAM, we observed a nearly vertical line on the van Holde-Weischet plot indicating a single species of oligomers. Mutation of either residues D16K/D17R or D33K/D34R results in more sigmoidal shaped curves. These curves cover a wider range of sedimentation coefficients with a drop in the lower bound as well as an increase in the upper bound indicating the presence of both smaller and larger oligomers compared to the WT. The D33K/D34R variant also has species with higher sedimentation coefficients than the D16K/D17R variant indicating stronger enhancement of oligomerization. The largest shift in oligomerization was observed after introducing both pairwise mutations (SAMsurf), with an extreme increase in the maximum range of sedimentation coefficients. This recapitulates the open-ended oligomerization observed with the SAM alone or attached to PHC3L. Importantly, these effects are dependent on the SAM polymerization interfaces, because mutating the EH SAM-SAM interface in the SAMsurf mutant reverts the protein to low S-values and homogeneous behavior. Thus, introducing charge complementarity between PhL and the SAM allows extensive oligomerization, similar to the effect of replacing PhL with PHC3L. Integrating the findings of multichain simulations of the SAM variants with the AUC analysis, the increase in oligomerization for variants D16K/D17R and D33K/D34R could be because of both the increase in linker-SAM and SAM-SAM interactions (**Fig. 3B+C**). Because SAM-SAM clustering is not observed for the SAMsurf mutant, increased oligomerization of this protein can be attributed to linker-SAM interactions.

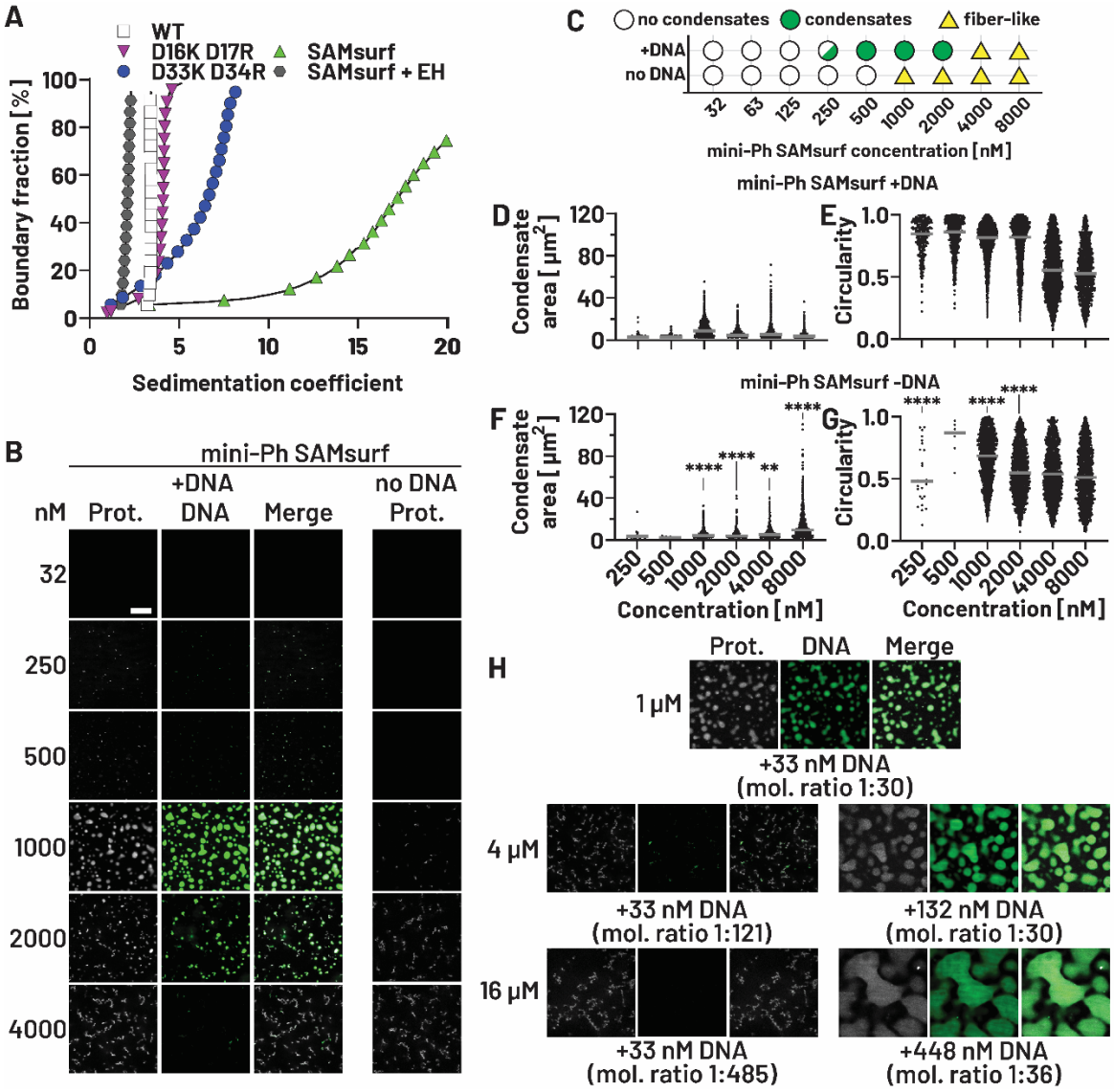

Figure 4: Introducing charge complementarity between PhL and SAM promotes oligomerization and phase separation. A. Analytical ultracentrifugation (AUC) of PhL-SAM with different SAM mutations. AUC is used to measure oligomerization, reflected as a concentration-dependent increase in sedimentation velocity. Thus, Ph linker paired with D16K D17R D33K D34R SAM mutant (=SAMsurf) oligomerizes more strongly than wild type. Mutation of the SAM oligomerization interface (EH) in this mutant abolishes oligomerization, indicating that it depends on specific SAM-SAM interactions. B. Images from mini-Ph SAMsurf titrations after overnight incubation. Proteins were labelled with Cy3 and DNA (33 nM, 156 bp dsDNA) visualized with YOYO1. Scale bar: 20 µm. C. Summary of titration experiments demonstrating that droplets form over a limited concentration window, and DNA is required for them. Fibrous aggregates form at higher concentrations or without DNA. D-G. Graphs of area and circularity of condensates from three experiments. Grey bars indicate median values. Data in all graphs was compared using Dunn's test for multiple comparison (**: $p<0.01$, ****: $p<0.0001$). Indicated comparisons were +DNA vs -DNA (i.e. D vs. F, E vs. G). H. Titrations of mini-Ph SAMsurf with DNA demonstrate that droplet versus fiber formation depends on the protein-DNA ratio.

Charge complementarity between PhL and SAM promotes mini-Ph phase separation *in vitro*. To determine whether linker-SAM interactions can also contribute to phase separation *in vitro*, we prepared mini-Ph with the SAMsurf mutant and tested it in phase separation assays *in vitro*. Titrations indicate that phase separation occurs at ~2× lower concentrations than mini-Ph, but ~4× higher concentrations than mini-Ph-PHC3L (**Fig. 4C**), in line with *in silico* c_{sat} predictions (**Fig. 2H** and **3D**). mini-Ph SAMsurf shows complex behavior in phase separation assays with DNA. Large droplet-like condensates form over a narrow concentration range (1-2 μM under these conditions) (**Fig. 4B,D,E**). Above 2 μM, or without DNA, mini-Ph SAMsurf rapidly forms fibrous aggregates This is reflected by a drop in condensate circularity in **Fig. 4E,G**. In our protein titrations with DNA, DNA concentration is fixed, so that not only protein concentration, but also the ratio of protein to DNA change across the titration. To test whether phase separation depends on a precise ratio of protein to DNA, we titrated both protein and DNA, keeping the ratio of the two fixed. Under these conditions, increasing concentration of both components leads to formation of progressively larger condensates, which can fuse and wet the glass surface (**Fig. 4H**). Thus, PhL-SAM interactions driven by charge complementarity in the SAMsurf mutant increases phase separation propensity, changes the underlying mechanism, and makes condensate properties highly dependent on the protein-DNA ratio.

Linker interactions affect condensate dynamics. Our data suggest linker interactions affect phase separation mechanism and condensate properties (shape, fusion and glass wetting). To assess condensates formed with each mini-Ph protein in more detail, we collected time series of condensate formation starting 30 min after initiating the reactions (**Fig. 5A, Sup. Movie 1**). The pattern of condensate formation is distinct for each protein. mini-Ph forms large round condensates that contain both protein and DNA. Fusion of large condensates is observed, often simultaneous with glass wetting. mini-Ph PHC3L forms small round condensates that fuse but rarely wet the glass surface under these conditions. Protein and DNA signals are heterogeneous—some condensates have strong signal for both, but condensates with strong protein signal and weak DNA signal (and more rarely the reverse) are also observed. mini-Ph SAMsurf initially forms fibrous structures with no DNA signal. As DNA is incorporated, condensates become more round and wet the surface.

To measure condensate dynamics, we carried out FRAP experiments on both protein and DNA in condensates (**Fig. 5B,C**). For mini-Ph PHC3L, we also analyzed condensates without DNA. FRAP data were fit with a double exponential (except for mini-Ph PHC3L), and parameters for both slow and fast recovering populations were calculated. At least 50% of the protein is mobile (recovers) for all three mini-Ph proteins (**Fig. 5C,D**). For PHC3L, the mobile fraction is lower than for mini-Ph in DNA containing condensates, and higher than mini-Ph for condensates without DNA. Recovery was variable for mini-Ph SAMsurf (**Fig. 5D**, **Sup. Fig. 4C,G,K**). mini-Ph PHC3L without DNA and mini-Ph SAMsurf had lower fractions of fast recovering protein (**Fig. 5D**), although fast τ was the same for all three variants (**Sup. Fig. 4A,F**). The τ of the slow recovering population was higher for mini-Ph SAMsurf, but not significantly different for mini-Ph PHC3L, either with or without DNA (**Sup. Fig. 4A,G**). Among the condensates formed by mini-Ph variants, DNA has the highest mobile fraction with mini-Ph PHC3L, while mobile DNA fractions with mini-Ph WT and SAMsurf mirror the mobile fractions of the protein (**Fig. 5E**).

We also carried out FRAP experiments on condensates formed by PHC3L-SAM. Protein recovery is not observed for these condensates (**Fig. 5B,C**). As a control, we tested the effect of adding DNA to PHC3L-SAM (which lacks the FCS domain that binds nucleic acid). Surprisingly, DNA is

incorporated into the PHC3L-SAM condensates (**Fig. 5B**). Addition of DNA slightly increases the recovery of PHC3L-SAM (**Fig. 5C,D**), while DNA recovers rapidly after bleaching (**Fig. 5C,E**). This result suggested that PHC3L might bind DNA, allowing it to be incorporated into condensates. To test this possibility, we carried out EMSAs with PHC3L-SAM, PhL-SAM, and PhL-SAMsurf. PHC3L-SAM, but neither of the other proteins, binds DNA (**Sup. Fig. 4L**). Thus, PHC3L makes 3 types of contacts absent with PhL: linker-linker, linker-SAM, and linker-DNA.

Linker interactions affect condensate formation in cells. Our *in vitro* and *in silico* experiments suggest that linker interactions, including between linker and SAM driven by charge complementarity, promote SAM oligomerization and SAM-dependent phase separation, and alter the properties, including size, of mini-Ph-DNA condensates. Linker-SAM interactions naturally occur with PHC linkers and can be induced for PhL by SAM surface mutations. To determine how the linker and linker-SAM contacts affect condensate formation in cells, we used live imaging to analyze condensate formation by Venus-tagged mini-Ph variants transfected into *Drosophila* Kc167 cells (**Fig. 6A**). Using *Drosophila* S2 cells, we previously found that Venus-mini-Ph forms condensates in a small fraction of cells, and it nearly always forms a single large condensate that excludes chromatin[75]. This pattern was confirmed in Kc167 cells (**Fig. 6A**). Venus-mini-Ph SAMsurf forms more condensates than mini-Ph WT (typically several per cell), and the condensates are smaller (**Fig. 6B, C**). We tested Venus-mini-Ph-PHC3L, as well as Venus-mini-Ph with PHC1L or PHC2L. Condensates formed with PHC linkers show a trend to be more numerous and smaller compared to the WT protein (**Fig. 6A-C**). These observations are in agreement with the predictions from simulations in **Fig. 2** and **3** as well as with *in vitro* phase separation assays (**Fig. 1** and **4**), all of which support an inverse correlation between SAM oligomerization and condensate size. We conclude that charge complementarity between linker and SAM, achieved either by mutating the SAM or by changing the linker, changes condensate formation in cells in a manner consistent with *in vitro* analysis and simulations.

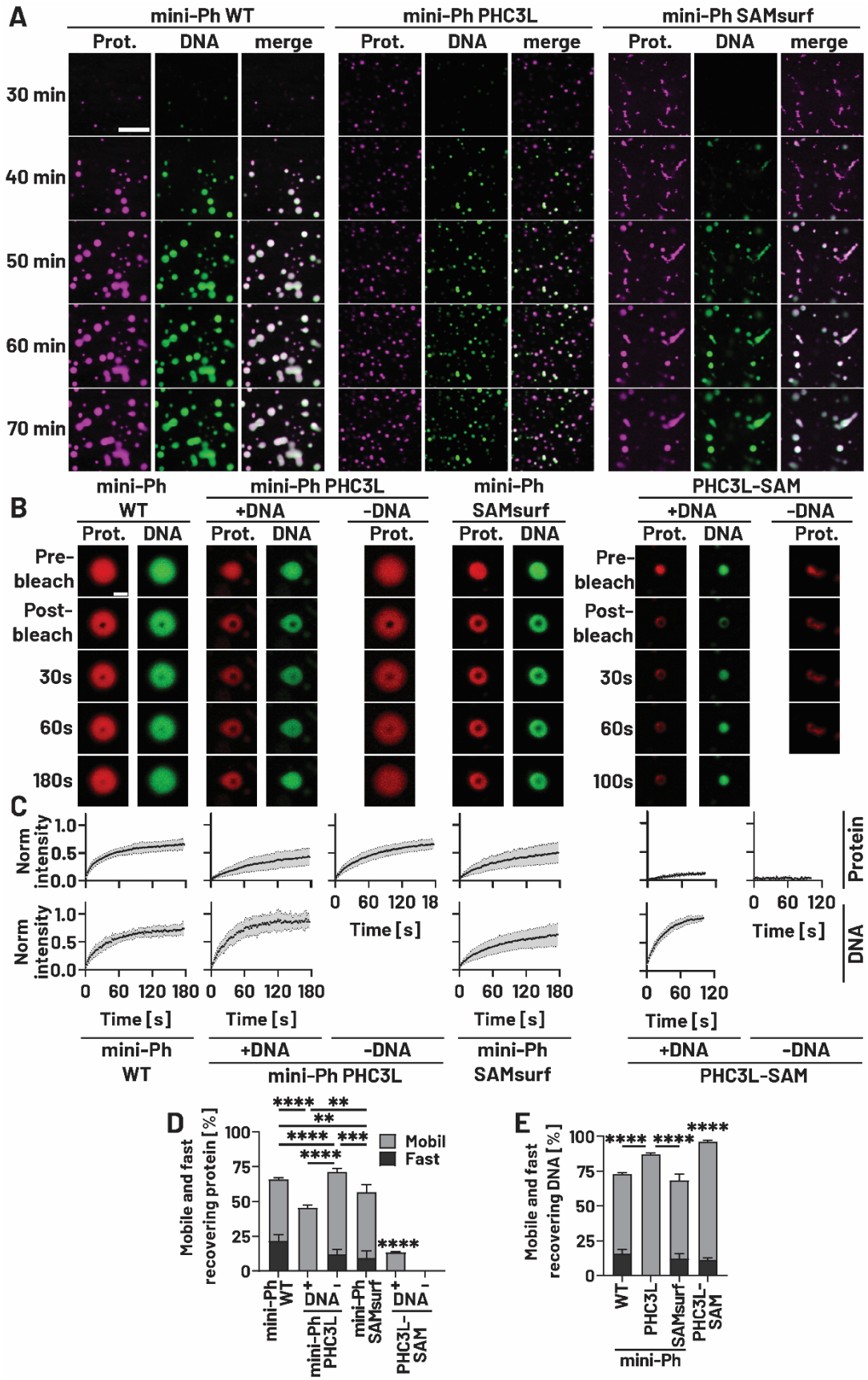

Figure 5: Linker interactions affect progression of condensates and condensate internal dynamics. A. Condensate formation by mini-Ph variants over time. Elapsed time after reaction start is indicated. Scale bar: 20 µm. B. Representative images from fluorescence recovery after photobleaching (FRAP) of mini-Ph variants and PHC3L-SAM. Proteins (4 µM) were labelled with Cy3 (mini-Ph) or Alexa 647 (PHC3L-SAM) and DNA (66 nM, except 132 nM for mini-Ph SAMsurf, 156 bp dsDNA) visualized with YOYO1. Scale bar: 3 µm. C. Summary of FRAP experiments. The curves represent fits of the combined data for each condition ($n \geq 8$) with standard deviations indicated as shaded area. PHC3L-SAM without DNA did not recover. D, E. Mobile and fast recovering protein (D) and DNA (E) fractions were affected by changes in linker interactions. The parameters were obtained from the fits in C with error bars representing standard deviations. Mobile fractions in all graphs were compared using Dunnett's T3 test for multiple comparison (**: $p<0.01$, ***: $p<0.001$ ****: $p<0.0001$). Asterisks for PHC3L-SAM refer to comparisons to all other conditions.

We previously showed that the large, disordered N-terminal region of Ph, which is not present in mini-Ph, or the main isoform of PHC2, affects the number and properties of condensates that Ph forms[72,75]. To determine whether linker-SAM charge complementarity remains relevant in the full-length protein, we overexpressed full length Venus-Ph variants. We also tested Venus-PHC3, which has a distinct N-terminal region (**Fig. 6D**). In comparison to the WT protein, a larger fraction of condensates formed by Ph-SAMsurf and Ph-PHC3L (as well as PHC3) are cytoplasmic (**Fig. 6E**). The ability of these proteins to aggregate and phase separate in the absence of DNA may explain these cytoplasmic condensates—they may form immediately after the protein is translated, before it can be imported to the nucleus. The nuclear condensates formed by these proteins were significantly smaller than those formed by Ph WT (**Fig. 6F**). Thus, linker-SAM interactions driven by charge complementarity, and the nature of the linker, are relevant in cells in the context of the full Ph protein.

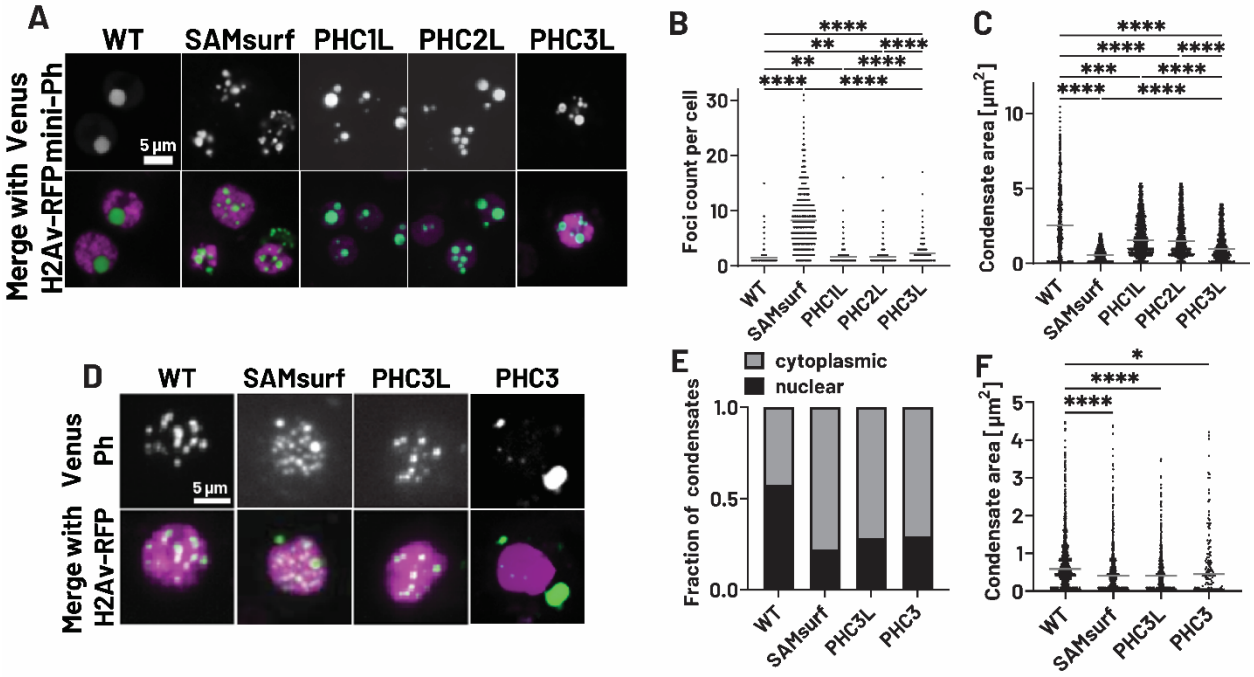

Figure 6: Altering charge complementarity and linker-SAM interactions affects condensate formation in cells. A. Representative images of overexpressed Venus-mini-Ph variants in Kc-167 cells. B, C. Quantification of condensate count per cell (B) and size (C). Data are compiled from three experiments. WT n=870 cells, 658 foci; SAMsurf n=842 cells, 5988 foci; PHC1L n=1004 cells, 1308 foci; PHC2L n=1036 cells, 1476 foci; PHC3L n=660 cells, 1451 foci. Representative images of overexpressed full-length Venus-Ph variants and Venus-PHC3 in Kc-167 cells. E. Cytoplasmic vs. nuclear condensate fractions. F. Quantification of nuclear condensate size from images in D. WT n=693 cells, 1431 nuc. foci, 2524 foci; PHC3L n=4346 cells, 586 nuc. foci, 2176 foci; SAMsurf 2131 cells, 888 nuc. foci, 1627 foci; PHC3 n=545 cells, 124 nuc. foci, 467 foci. Data in all graphs was analyzed with Dunn's test for multiple comparison (*: $p<0.05$, **: $p<0.01$, ***: $p<0.001$, ****: $p<0.0001$).

The linker affects Ph function in *Drosophila* imaginal discs. Previous work demonstrated that *Drosophila* imaginal discs are sensitive to *ph* levels and activity[40,79]. Overexpressing wild type Ph or Ph with a synthetic linker that enhances polymerization suppresses growth[40]. In contrast, deleting *ph* or impairing SAM polymerization results in tumorous overgrowth[40,79]. To test the effect of the linker and charge complementarity on Ph function, we expressed wild type Venus-Ph, Venus-Ph-SAMsurf, Venus-Ph-PHC3L or GFP only. We used *hedgehog*-Gal4 and *tubulin*-Gal80ts, which drives expression in the posterior compartment of wing imaginal discs at the permissive temperature (**Fig. 7A**). We induced protein expression by temperature shift for 24 hours before harvesting imaginal discs. This mild induction of Ph proteins was used to ensure that wing disc morphology was relatively normal. We measured the ratio of posterior compartment to total disc size. For discs expressing PhWT or GFP, this ratio is ~0.5 (**Fig. 7 A,B,H**). Discs expressing Ph-SAMsurf, or Ph-PHC3L have a reduced ratio (**Fig. 7 D,F,H**). This is consistent with growth suppression in cells expressing these proteins. Thus, changing linker interactions, which affect phase separation and oligomerization propensity, affects growth control by Ph.

We were able to image condensates formed by different Ph proteins in wing disc cells (**Fig. 7 C,E,G**). Similar to what was observed in cultured cells (**Fig. 6**), the sizes of condensates in Ph SAMsurf and Ph PHC3L are significantly smaller compared to Ph WT condensates as quantified in **Fig. 7I**. Taken together, linker interactions change both condensate properties and Ph function during development.

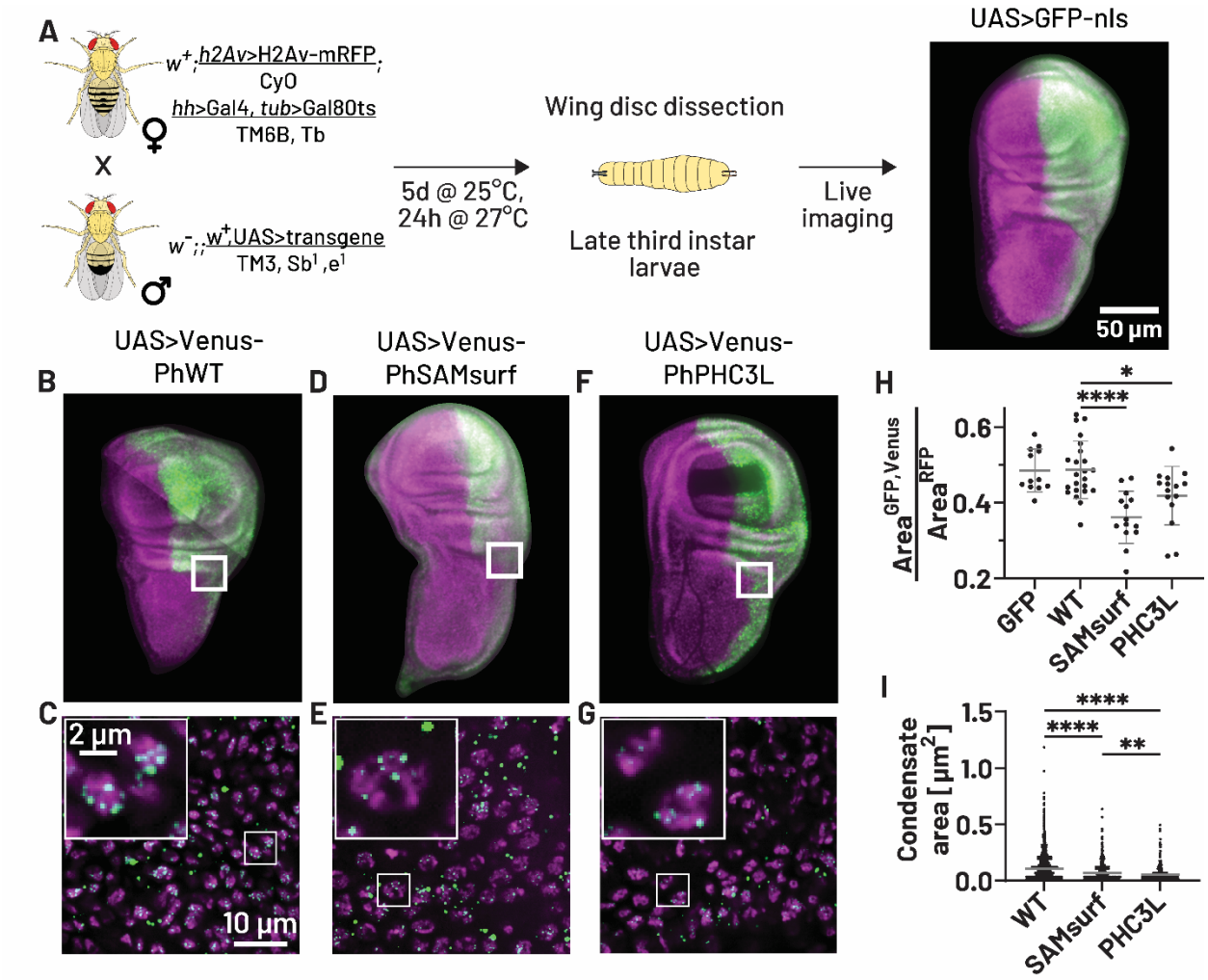

Figure 7: Altering charge complementarity and linker-SAM interactions affects Drosophila wing imaginal disc development. A. Schematic of fly experiments with fly genotypes and experimental procedure indicated. B-G. Representative wing discs (B,D,F) and zoom on corresponding cells (C,E,G) from flies expressing Venus-Ph transgenes under control of UAS promoter driven by hedgehog-Gal4 with tubulin-Gal80ts. Images in B, D, F are summed z-projections on a black background to aid visualization. The nuclear marker is H2Av-RFP expressed by the ubiquitin promoter. H. Quantification of the ratio of posterior compartment to total disc area. GFP: n=12; WT: n=23; PHC3L: n=14; SAMsurf: n=15. I. Quantification of condensates in wing disc cells indicates reduced size for Ph PHC3L and Ph SAMsurf similar to cell culture experiments. n values (# discs analyzed) WT=6; PHC3L=5; SAMsurf=9. Data in all graphs were analyzed with Dunn's test for multiple comparison (*: $p<0.05$, **: $p<0.01$, ****: $p<0.0001$).

Discussion

We investigated how the disordered linker that connects Ph SAM to Ph affects the phase separation and oligomerization activities of the SAM. By comparing the linker sequences of Ph in *Drosophila* and its human homolog PHC3, which (unlike the SAM), are not conserved, we unraveled the mechanistic basis of how the linker influences SAM oligomerization and SAM-dependent phase separation. Our results highlight the importance of linker-SAM interactions in controlling the Ph SAM activities both *in vitro* and *in vivo*.

We propose a charge complementarity model to explain our key findings. According to this model, opposing charges in the linker sequence and on the SAM surface facilitate interactions, which enhance SAM oligomerization and phase separation. This model is supported by our experiments, including analytical ultracentrifugation (AUC) with PHC3L-SAM and PhL-SAMsurf, as well as phase separation assays with their mini-Ph equivalents. In contrast, when charge complementarity is absent, both the oligomerization and phase separation activities of the SAM are restricted, as shown by our previous[75] and current *in vitro* experiments with the PhL and SAM.

Charge complementarity cannot fully explain our results, since PHC3L has a stronger effect on condensates than the SAMsurf mutations. Our simulations suggest that linker-linker interactions by PHC3L contribute to phase separation behavior, while experimental data indicate that PHC3L also binds DNA. Differences between PHC3L and SAMsurf are more obvious in condensate formation assays than in AUC measures of polymerization. While this may reflect technical differences in the assays, condensate formation assays, but not AUC or MD, include the HD1 and FCS domains. It is thus possible that these domains also interact with PhL, PHC3L, or the SAM.

A model for linker-controlled phase separation. Taking all of our data together, we have identified multiple interactions and determined how they contribute to Ph SAM polymerization and phase separation (summarized in **Fig. 8**). Two classes of SAM-SAM interactions can occur—canonical interactions involved in polymerization, and non-canonical (weak) SAM-SAM interactions. Weak SAM-SAM interactions are observed in simulations and are altered by SAM surface mutations. These non-canonical interactions may account for our previous observation that mini-Ph without the SAM does not phase separate *in vitro*, but mini-Ph with the SAM polymerization interface mutated does[75]. In contrast, polymerization is eliminated by mutations in the canonical interface, indicating that weak SAM-SAM interactions do not contribute significantly to the polymerization measured in AUC assays (**Fig. 4A**). In mini-Ph, the FCS interacts with DNA; whether other protein-protein interactions occur with HD1 and FCS is not known. When PHC3L is present, three additional types of interactions occur—linker-SAM, linker-linker, and linker-DNA.

Our data are consistent with the following model. In the case of *Drosophila* mini-Ph, SAM-SAM interactions are restricted by the Ph linker (through a mechanism we have not yet elucidated) so that mini-Ph forms short oligomers. PhL does not interact with itself or with the SAM so that mini-Ph alone has insufficient interactions to drive phase separation at the concentrations obtained for experiments. In the presence of DNA, which binds to the HD1/FCS region, mini-Ph readily undergoes phase separation. We anticipate that binding of multiple mini-Ph molecules to individual DNAs provides additional multivalency to drive phase separation. In the case of PHC3L, both linker-linker and linker-SAM interactions provide multivalency and shift the boundary for phase separation to much lower concentrations. DNA is no longer required for phase separation, and

indeed inhibits formation of drops; whether this is partly due to linker-DNA interactions remains to be determined. Thus, phase separation driven by PHC3L utilizes a different pathway—confirmed by the absence of requirement for FCS or HD1. In this case, linker-SAM and linker-linker interactions provide the multivalency. The SAMsurf mutant adds linker-SAM, but not linker-linker interactions, and removes weak SAM interactions. Linker-SAM interactions do not allow phase separation without the HD1/FCS region and DNA. However, when HD1 and FCS are present, linker-SAM interactions cause mini-Ph SAMsurf to readily form fibers without DNA. In the presence of DNA, mini-Ph SAMsurf can instead form drops, but droplet formation is highly sensitive to the ratio of protein to DNA. Thus, simply increasing polymerization with linker-SAM interactions restricts the conditions under which phase separation occurs, while adding both linker-SAM and linker-linker interactions (and retaining non-canonical SAM-SAM interactions) allows phase separation under a much broader range of conditions (lower concentrations, without HD1/FCS, and with or without DNA). Although speculative, this could rationalize why the linker has changed over evolution, rather than the SAM-SAM interface or the SAM surface. It is intriguing to note that in developing *Drosophila* larvae, the SAM surface mutant shows the largest variability in terms of its impact on disc growth regulation.

Previous experiments showed that PhL restricts oligomerization of Ph SAM, both in mini-Ph and as a linker-SAM construct. Our experiments do not reveal the mechanism of inhibition, since simulations do not predict PhL-PhL or PhL-SAM interactions. It is possible that non-complementarity between the charge of PhL and SAM restrict oligomerization. Mini-Ph forms short polymers, 4-6 units, so oligomerization is restricted to one turn of the polymer helix. In the context of the polymer, the PhL will be more constrained than in a monomer. PhL may thus form a negative charge cloud around the polymer that repels incoming monomers or polymers.

It is interesting to note that PRC1 is implicated in the formation of both very long[80] and short range (sub-TAD)[81] chromatin interactions in mammals. The pattern of PRC1 binding also differs in mammals versus *Drosophila*. In *Drosophila*, PRC1 localizes to discrete peaks, many of which are Polycomb Response Elements—dense arrays of binding sites for TFs that can recruit PcG proteins. In contrast, PRC1 localizes more broadly over regulatory regions and genes in mammals, where distinct recruitment mechanisms may predominate. We hypothesize that the much wider range of concentrations over which PHC3L-driven condensates form, and their ability to form either with or without DNA can accommodate functions over a larger size range. It is also interesting that in the PHC1 and PHC2 linkers, 3 residues that are negatively charged in PHC3L are instead serines, and thus could form charge-mediated contacts in a phosphorylation dependent manner. In contrast, the restricted polymerization of Ph in *Drosophila* cells may be well suited to punctuated binding and discrete interactions between bound sites. The interactions defined here will allow us to test this hypothesis in future experiments, by engineering PHC3-like behavior in *Drosophila* Ph and Ph like behavior in PHCs.

In summary, our work describes a mechanism by which Ph SAM activity has changed over evolution while preserving overall protein architecture through changes in the linker (an IDR). These results suggest the precise activity of the SAM may be relevant to Ph function in chromatin organization. More broadly, they provide an example of how IDRs and oligomerizing domains function together in protein phase separation.

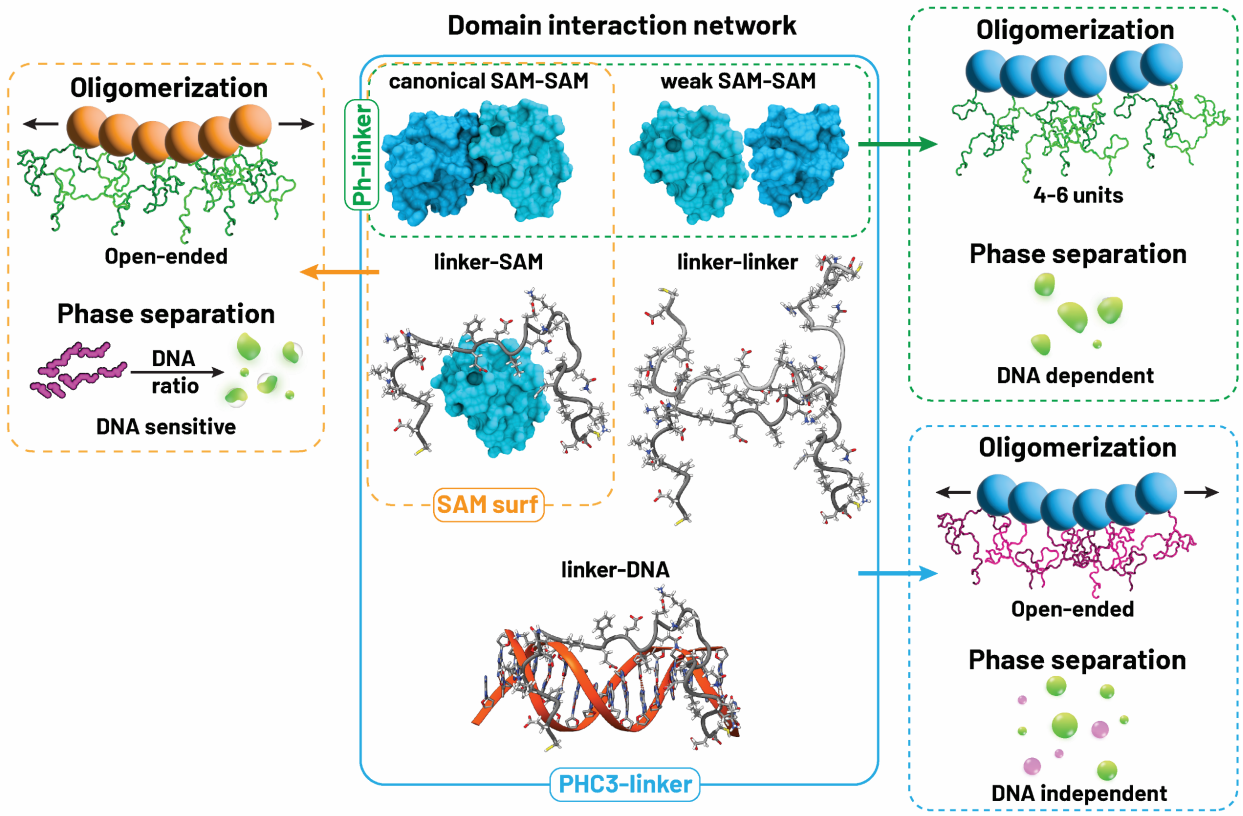

Figure 7: Model of *linker and SAM* interactions in mini-Ph. *Mini-Ph WT has* canonical SAM-SAM, and weak SAM-SAM interactions. Condensate formation in vitro depends on DNA, and oligomerization is limited. mini-Ph SAMsurf loses weak SAM-SAM interactions but gains linker-SAM. Phase separation in vitro is sensitive to DNA forming fiber-like aggregates at high protein/DNA ratio and droplet-like condensates with higher amounts of DNA. The protein exhibits strong oligomerization activity. mini-Ph PHC3L has all interactions present in mini-Ph *WT* and mini-Ph SAMsurf, as well as linker-linker and linker-DNA. Condensate formation is independent of DNA and occurs at low concentrations. The human linker promotes oligomerization.

Limitations

The study primarily relies on simplified model systems, such as chimeric proteins and *in vitro* assays, to investigate the effects of the linker sequence on phase separation and condensate properties. While our *in vitro* approaches offered controlled experimental conditions, they may not fully capture the complexity and dynamics of the native cellular environment. Our *in vivo* experiments, while able to show differences based on the sequence of the linker/SAM, all rely on overexpression. Future experiments manipulating the sequence of endogenous Ph or PHCs will be needed to measure the impact of linker-SAM interactions on gene regulation and chromatin organization.

Acknowledgements

The authors thank members of the Francis lab and Dr. François Robert for critical reading of the manuscript. We thank Dr. Dominic Filion for assistance with microscopy. We thank Dr. Utkarsh Kapoor for input and preliminary simulations and Drs. Stefan Niekamp and Robert Kingston for sharing unpublished work. We are grateful for the computation resources provided by Texas A&M High Performance Research (HPRC).

This work was supported by: the Canada 150 Research Chairs program (C150-2017-00015, BD), the CFI (CFI-37589, BD), the NIH (1R01GM120600, BD), (R01GM114338 to CAK & NJF), (R15CA26780, CAK), (R01GM136917, JM), NSERC (DG-RGPIN-2019-05637, BD), the CIHR (469023, NJF), and) and the Welch Foundation (Grant A-2113-20220331, JM). UltraScan supercomputer calculations were supported through NSF/XSEDE grant TG-MCB070039N, and University of Texas grant TG457201 to BD. AH was supported by a scholarship grant from NSERC and TMG by doctoral fellowships from FRQS and the IRCM (Jacques-Gauthier Tribute Scholarship). YCK is supported by the Office of Naval Research through the U.S. Naval Research Laboratory base program.

Author Contributions

TMG: conceptualization, investigation, visualization, writing—original draft; RMR: conceptualization, investigation, visualization, formal analysis, writing—original draft; AJM, HJL, AH: investigation; TMP: visualization, formal analysis, writing—review & editing; YCK: investigation, formal analysis; BD & CAK: conceptualization, resources, supervision, funding acquisition; JM: conceptualization, writing-original draft, funding acquisition, supervision; NJF: conceptualization, resources, writing—original draft, supervision.

Declaration of interests

The authors declare no competing interests.

Methods

Cloning: To express Venus-tagged proteins in Kc cells, mini Ph or full length Ph variants were first cloned into a house-modified Gateway donor vector using Gibson cloning (HiFi Assembly, NEB) or restriction-ligation cloning. Sequences were confirmed before using Gateway LR recombination (LR Clonase II, Thermo Fisher) with pHVW (DGRC stock # 1089) for heat shock inducible expression in *Drosophila* cells. Similarly, mini Ph constructs were subcloned into a Gateway destination vector (pFBFG, lab made) for baculovirus-mediated recombinant protein expression in Sf9 cells. Linker SAM variants with N terminal HisSUMO-tag were assembled in a pET vector (starting from Addgene Plasmid #111559) for recombinant expression in *E. coli* using Gibson assembly. Venus-tagged *ph* transgenes from pHVW plasmids were subcloned into pUASt-attB vector using Gibson cloning for PhiC31 mediated generation of transgenic *Drosophila*.

Protein purification: mini Ph variants were purified from whole cell extracts of Sf9 cells infected with baculoviruses for 3 days. Whole cell extracts were prepared in buffer F (20 mM Tris pH 8, 500 mM NaCl, 20% glycerol, 4 mM MgCl2, 0.4 mM EDTA, 0.4 mM PMSF, 2 mM DTT, 0.1% NP 40) using a Dounce homogenizer. Extracts were incubated with M2 anti-FLAG agarose beads (Sigma-Aldrich) overnight, and then washed by gravity flow with increasingly stringent BC buffers (20 mM HEPES pH 7.9, 20% glycerol, 0.4 mM EDTA, 0.2 mM PMSF, 1 mM DTT, 0.05% NP 40, 10 µM ZnCl2) containing 300 mM KCl, 600 mM KCl and 1200 mM KCl (20 bead volumes per wash step). The salt concentration was reduced in reverse order after a stringent wash consisting of BC2000N + 1 M Urea (20 mM Hepes, pH 7.9, 2 0.4 mM EDTA, 2 M KCl, 1 M deionized urea, 0.05% NP40, no glycerol). Prior to eluting the protein with 0.4 mg/ml FLAG peptide in BC300 without NP 40, anti-FLAG beads were incubated with 5 volumes of BC300N with 4 mM ATP + 4 mM $MgCl_2$ for 30 min at room temperature to reduce the amount of HSC-70 that may otherwise copurify. Concentrated protein at 1-2 mg/ml was stored at −80 °C in BC300. In all purifications from Sf9 cells the following concentrations of protease inhibitors were added to buffers: Aprotinin 10 µg/ml, Leupeptin 10 µg/ml, Pepstatin 2 µg/ml, TLCK 50 µg/ml, and 1.6 µg/ml Benzamidine. For mini-Ph-PHC3L and mini-Ph SAMsurf, a modified protocol was used for some preparations, which increased the protein yield. In side-by-side comparisons, proteins prepared with both protocols behaved similarly. The protocol is as above but with the following changes. $MgCl_2$ was used at 10 mM in the extraction and all washes up to the ATP-$MgCl_2$ wash. Before incubating the extracts with beads, PEI precipitation was used to deplete nucleic acids. A 5% PEI (pH 8) solution was added to a final concentration of 0.1%. Extracts were mixed and immediately centrifuged for 10 min at 15,000g. The supernatant was added to anti-FLAG resin. Proteins were eluted with 0.1M Glycine, pH 3 instead of FLAG peptide. Elutions were immediately neutralized with 1M Tris pH 8.5 (added at 1:20), and proteins were dialyzed through three changes of BC300 before concentrating at room temperature to 1-2 mg/ml and storing at -80 °C.

HisSUMO-tagged Linker-SAM proteins were expressed in BL21(DE3) LOBSTR-RIL cells. Cultures were grown at 37 °C to an OD of 0.6, and then shifted to 18°C for overnight induction with 1 mM IPTG. Cells were pelleted, washed once in ice cold PBS with 1 mM PMSF, flash-frozen, and stored at −80 °C. Cells were resuspended in 2 ml/g lysis buffer (50 mM Tris, pH 8.5, 500 mM NaCl, 10 mM β-ME, 1 mM PMSF, 1 mM EDTA). 1 mg/ml lysozyme was added and cells were incubated for 1 h at 4°C on a nutator. Afterwards, cells were flash-frozen in liquid nitrogen, thawed at 37 °C, and sonicated in an ethanol ice bath for 5x30 s (30 s off cycle) at 40% intensity. Freeze–thaw and sonication were repeated three times, and the lysate was centrifuged for 1 h at

48,400g and 4 °C. Cleared lysate was filtered through a 22-µm filter. Filtered lysate was applied to a 1-ml His-Trap (all FPLC columns were obtained from GE Healthcare) column using an ÄKTA FPLC, and eluted with a gradient of Imidazole (from 20 mM to 1 M) in binding buffer (50 mM Tris, pH 8.5, 500 mM NaCl for PHC3L/1 M for PhL, 10 mM β-ME, 1 mM PMSF). Fractions with recombinant protein were pooled and dialyzed overnight against binding buffer. The eluted fraction were further purified by size-exclusion chromatography using a Superdex 200 column, then concentrated to at least 1 mg/ml, flash frozen and stored at −80 °C.

For cleaving HisSUMO-tag, His-tagged SUMO protease Ulp1 was expressed in BL21(DE3) Rosetta cells. Cultures were grown at 37 °C to an OD of 0.5 and protein expression was induced with 1 mM IPTG for 3 h. Cells were pelleted, resuspended in 4 ml/g lysis buffer (50 mM NaH2PO4, 300 mM NaCl, 10 mM Imidazole, pH 7.5). 1 mg/ml lysozyme, 1 mM MgCl2 and Benzonase were added and cells were incubated for 30 min on ice. Cells were sonicated for 10x30 s (30 s off cycle) in an ethanol ice bath at 40% intensity. The lysate was cleared for 25 min at 48,400g and 4 °C, before it was applied on a Ni NTA agarose beads (QIAGEN) equilibrated in lysis buffer. Lysate was passed over the beads by gravity flow four times, then washed with 10 bead volumes wash buffer (50 mM NaH2PO4, 300 mM NaCl, 20 mM Imidazole, pH 7.5) before the protein was eluted with 3 volumes elution buffer (50 mM NaH2PO4, 300 mM NaCl, 250 mM Imidazole, pH 7.5). Fractions containing Ulp1 were pooled, flash frozen and stored at −80 °C.

Fluorescent labelling of mini Ph variants and PHC3L-SAM: NHS-ester-Cy3 was used to randomly label lysines in mini Ph proteins (Alexa647 for PHC3L-SAM). Labeling was carried out with a 0.5:1 (dye:protein) ratio for 1 h at room temperature. Labeling was quenched by addition of lysine to 10 mM. Free dye was removed using a Zeba column equilibrated in BC300 buffer (20 mM Tris, pH 8.5, 300 mM NaCl for PHC3L-SAM). For PHC3L-SAM, the His-SUMO tag could be labelled too, so it had to be removed by cleavage with Ulp1. Cleavage was conducted for 1 h at 37 °C, after which samples were transferred to pre-equilibrated Ni NTA agarose beads (QIAGEN) (same buffer as above). After binding for 1 h at room temperature, the supernatant was recovered containing the labelled PHC3L-SAM construct. His-SUMO and Ulp1 (also His-tagged) remained remained bound to beads. Labeled protein was mixed with unlabeled at a ratio of between 1:5 to 1:10, depending on the labeling efficiency, for imaging experiments.

Test for DNA contamination in protein preparations: Protein preparations used in phase separation assays were tested for contamination with nucleic acid. Protein samples were digested with proteinase K overnight at 37 °C. The samples were loaded on a 1% agarose gel and run for 30 min at 100V. The gel was stained with highly sensitive SybrGold dye before imaging.

Proteins for AUC: The DNA sequence matching Ph residues 1397 – 1577 comprising the Ph linker + SAM was cloned into a modified pET-3c plasmid following an N-terminal leader sequence of MHHHHHHAMKGVDSPSAELDKKAENLYFQGTR. All mutation were introduced using the QuikChange Lightning Site-Directed Mutagenesis Kit (Agilent). The DNAs were transformed into BL21-Gold(DE3) pretransformed with pLysSRARE2 and induced overnight at 15° C using 1 mM IPTG. Bacterial cells collected from 1 L of culture were resuspended with 10 mL of a lysis buffer (50 mM Tris pH 8.0, 150 – 200 mM NaCl, 20 mM Imidazole, 5 mM βME, 1 mM PMSF). For the D16K D17R D33K D34R protein with the oligomer interface mutant, 20 mM ADA pH 6.0, 50 mM NaCl, 1 mM βME was used as the lysis buffer. Cells were lysed via sonication and the soluble lysate introduced to 1 mL of bulk Ni-sepharose beads (Cytiva). The beads were exposed to the soluble lysate with gentle agitation for 30 – 60 min at room temperature then washed several times

with the lysis buffer (minus PMSF) using a total volume 30 – 50X the Ni-sepharose volume. The bound proteins were eluted with 300 mM Imidazole pH 6.9 – 7.5, 150 mM NaCl, 5 mM βME. For the D16R D17R D33K D34R oligomer interface mutant, the elution buffer was 20 mM ADA pH 6.0, 50 mM NaCl, 1 mM βME. After the bulk Ni-affinity purification, all proteins except the two having the D16K D17R D33K D34R mutations were further purified using anion exchange chromatography (HiTrap Q, Cytiva) running a gradient from 0% of 25 mM tris pH 8.0 – 8.5, 50 mM NaCl, 5 mM βME to 100% of 25 mM tris pH 8.0, 1 M NaCl, 5 mM βME over 60 minutes. Cation exchange chromatography was used for the D16K D17R D33K D34R proteins, either with or without the oligomerization interface mutation, using a gradient of 0% 20 mM MES or ADA pH 6.0, 50 mM NaCl, 1 mM bME to 100% 20 mM Tris pH 8.0, 1 M NaCl, 1 mM βME over 60 minutes. The D16K D17R D33K D34R protein with the oligomer interface mutant was further purified over a HisTrap HP using a gradient of 0% 20 mM Tris pH 8.0, 200 mM NaCl, 5 mM βME to 100% 500 mM Imidazole pH 7.5, 200 mM NaCl, 5 mM βME over 60 minutes. For the AUC experiments, all proteins were diluted to 37 mM into a buffer of 10 mM Tris pH 8.0, 50 mM NaCl, 1 mM TCEP.

Phase separation assays: Proteins and DNA templates (obtained from PCR and/or gel extraction) were routinely centrifuged full speed in a microfuge for 2–5 min at 4 °C to remove aggregates before setting up phase-separation assays. For phase-separation assays, reactions (typically 15 µl) were assembled in a 384-well glass-bottom imaging dish (SensoPlate, Greiner Bio-One). Wells were not pretreated. Phase separation was initiated by addition of the protein to the reaction mix containing DNA and YOYO-1 (at 1:10000), and mixing the reaction by gently pipetting up and down three times without introducing air. Reactions were incubated in the dark for 15 min or up to overnight. Typical reaction conditions are 60 mM final salt, 20 mM HEPES, pH 7.9.

Phase separation of HisSUMO-Ph linker SAM or HisSUMO-PHC3 linker-SAM (diluted to salt concentration of 300 mM) were induced by addition of 1:10 molar ratio of Ulp1 in BC0, resulting in cleavage of the solubility tag as assessed with SDS PAGE. Reaction conditions were 56.25 mM final salt, 20 mM Tris, pH 8.5.

Time course experiments were conducted at 4 µM protein and 66 nM DNA (132 nM for mini-Ph SAMsurf reactions).

For FRAP experiments, phase separation reactions were setup as usual and protein/DNA concentrations were same as in the time course but with the following modifications. The reaction buffer was supplemented with an oxygen scavenger system composed of 10 mM DTT, 40 mM glucose, 20 µg/mL Glucose Oxidase and 3.5 µg/mL Catalase (as described in[82]). In the absence of oxygen scavengers, we did not observe protein recovery, and DNA recovery was variable, consistent with photodamage from the bleaching step.

Cell culture and live cell imaging: Wild-type *Drosophila* Kc 167 cells were cultured in M3 media (Sigma Aldrich) with 5% FBS and Penicillin/Streptomycin. For live-cell imaging, cells were plated at 2 million cells per well in 12-well plates the night before transfection. Transfection was carried out using Trans-IT lipid (Mirus), according to the manufacturer's protocol. 750 ng of each heat shock inducible Venus-(mini)Ph construct were transfected along with 250 ng of pAct5C-H2Av-RFP as a constitutive nuclear marker. One day after transfection, cells were replated on ConA-coated imaging dishes (Ibidi). Cells where heat shocked for 8 min at 37 °C to induce protein expression, and analyzed within 24 h after heat shock.

Transgenic *Drosophila* experiments: Venus-tagged *ph* transgenes subcloned into pUASt-attB vector were integrated into y[1] w[*] P{y[+t7.7]=nos-phiC31\int.NLS}X; P{y[+t7.7]=CaryP} attP2 flies by microinjection into early syncytial-stage blastoderm embryos (Genome ProLab, Sherbrooke, QC, Canada). This background contains both PhiC31 integrase on the X chromosome and an attP integration site on chromosome 3. Stable transformants were selected by integration of the *white* gene into *white* mutant background. Transgenic constructs of *ph* are controlled by the UAS promoter. Expression of Ph variants was driven by mating UAS transgenic flies with *hedgehog*-Gal4/*tubulin*-Gal80ts flies that also harbor *ubiquitin*-H2AvRFP as a nuclear marker. Crosses were kept at 25°C for 5 days before shifting to 27°C for 24 h. Larvae were collected in the mid to late L3 stage and wing imaginal discs were dissected and mounted in M3 medium for live imaging. For whole wing disc imaging, discs were mounted with spacers, while spacers were omitted for condensate imaging at high magnification.

Imaging: All images from mini Ph phase separation assays (except FRAP experiments), live-cell imaging and wing discs were collected on a Zeiss AxioObserver Z1 microscope, equipped with a Yokogawa CSU-1 spinning-disk confocal head. Zen 2012 software was used for image acquisition with a 63× oil objective for phase separation assays and cell imaging, 20x air objective for full wing disc and 100x oil objective for wing disc condensates, and an Evolve EMCCD camera from Photometrics. The excitation wavelengths for YOYO-1/Venus, Cy3/RFP were 488 nm and 561 nm, respectively. For linker-SAM proteins, images were collected using the differential interference contrast filter set on an LSM 710 AxioObserver Confocal Microscope from Zeiss with a 40x oil objective.

FRAP imaging was conducted using an LSM 710 AxioObserver Confocal Microscope from Zeiss with a 40x oil objective. Excitation wavelengths for YOYO, Cy3 and Alexa647 were 488 nm, 561 nm and 647 nm, respectively. Upon selecting a condensate, a circular region of interest (ROI) with a diameter of 1 µm was designated for bleaching. Bleaching at 456 nm with 70% laser power for 10 iterations at the lowest pixel dwell time resulted in simultaneous bleaching of all fluorophores. FRAP acquisitions were obtained within a window from ~10 min to around ~60 min after starting the reaction. Two images before, followed by acquisitions every 2 s after bleaching were captured for up to 180 s.

Image analysis of condensates: Exemplary images were prepared using Zen2 (blue edition) or ImageJ (Fiji[83]). The analysis pipeline in CellProfiler 4.2.5[84] used the original .czi acquisitions as input. The analyses were done on the protein signal (Cy3 channel). First, for background subtraction, the images were inverted and the module "Enhance Or Suppress Features" was used to enhance dark holes with a size range from 1 to 100 (1 to 20 for mini-Ph SAMsurf condensates) (rolling ball algorithm). Condensates were then identified using the two-class Otsu algorithm for global thresholding with a typical object diameter of 2 to 2000 and a lower bound for threshold at 0.001 (Minimum Cross-Entropy algorithm with 8 to 2000 size filter and lower threshold bound of 0.006 was used for mini-Ph SAMsurf condensates). Other options were deactivated. The total area covered by condensates as well as individual condensates sizes and shape were measured and exported. The form factor as a measure of shape obtained from CellProfiler may contain artifactual values bigger 1; these values were excluded and the measure is referred to as Circularity here. Statistics were calculated and graphs were plotted using GraphPad Prism 10, using recommended settings, including for correction for multiple comparisons.

FRAP analysis: Input .lsm files were analyzed in ImageJ[83]. First, protein (Cy3 or Alexa647) and DNA channels were split, and background was subtracted using the rolling ball algorithm with a radius of 50. Subsequent analyses were done with publicly available ImageJ plugins (developed by Jay Unruh, Stowers Institute for Medical Research, Kansas City, MO). First, "roi average subtract jru v1" and "roi average divide jru v1" with an ROI outside condensates (background subtraction) and an ROI in a non-bleached condensate (detrending) were used, respectively. Then, "create spectrum jru v1" was used on an ROI in the bleached area to obtain the FRAP trace that were saved as plot objects. Individual FRAP traces from each condition were then combined ("combine all trajectories jru v1") and normalized from 0 to 1 ("normalize trajectories jru v1" with Min_Max option). The normalized traces were then saved as .csv files. FRAP fits were done on the combined data, or on individual traces, in GraphPad Prism 10 using single or double exponential fits depending which model fits better (Sum-of-squares F test with default settings). The single and double exponential equations were as follows:

$$Y_{single} = Y_0 + (Plateau - Y_0) * (1 - e^{-\frac{x}{\tau}}) \quad (4)$$

$$Y_{double} = Y_0 + SpanFast * \left(1 - e^{-\frac{x}{\tau_{Fast}}}\right) + SpanSlow * \left(1 - e^{-\frac{x}{\tau_{Slow}}}\right)$$
$$with\ SpanFast = (Plateau - Y_0) * FractionFast$$
$$and\ SpanSlow = (Plateau - Y_0) * (100 - FractionFast) \quad (5)$$

Image analysis of live cells: Custom scripts were used in ImageJ to split channels from raw image files and convert them to Sum slices Z-projections. The red channel (RFP) was used to segment nuclei (thresholded with the Li algorithm). Thresholded images were converted to masks, processed with a watershed algorithm, and Analyze Particles used with a size threshold of 10-100 to select nuclei. The green channel (Venus fusion proteins) was then segmented (thresholded with Bernsen algorithm with a radius of 5, and parameters set to 0), and foci were selected with a size threshold of 1-100. Foci were separated into cytoplasmic vs nuclear using the nuclear mask generated before in combination with the BinaryReconstruct function of the Morphology plugin. Areas of thresholded foci were measured using Analyze Particles, size = 0-100. Statistics were calculated and graphs were plotted using GraphPad Prism 10, using recommended settings, including for correction for multiple comparisons.

Image analysis of wing discs: The input .czi stacks of individual wing discs were first split into RFP channel and Venus channel using CellProfiler. Split images were saved as .tif files and a custom ImageJ script was used to generate Sum slices Z-projections. The whole wing disc images (marked by nuclear H2Av-RFP) were transferred to Ilastik[85] for training a pixel classifier. Once the classifier achieved satisfying segmentation of full wing discs, all images were processed to obtain a simple binary segmentation output. The same was repeated for each condition, GFP control, Ph WT, Ph SAMsurf and Ph PHC3L, respectively. The masks of whole wing discs and corresponding protein expression domains were opened in CellProfiler, where they were resized with a factor of 0.5 (nearest neighbour interpolation). A manual threshold was used to identify wing disc and expression domain as objects, and to fill holes. After resizing the wing disc and expression domain back with a factor of 2, the size of each object was measured. Statistics were calculated and graphs were plotted using GraphPad Prism 10, using recommended settings, including for correction for multiple comparisons.

Image analysis of condensates in wing disc cells: Input .czi files were opened in CellProfiler. Both channels (RFP and Venus) were resized by factor of 2 (bilinear interpolation). The RFP channel was inverted and dark holes in a size range of 10 to 40 were enhanced (rolling ball background subtraction). Nuclei were then identified using the adaptive three classes Otsu algorithm (middle class as foreground) with an object size range 20 to 80 and an adaptive window size of 100. Objects touching the image border were excluded. The "Shape" mode was used for both declumping options, while other options were left at default. Next, speckles were enhanced in the Venus channel with a feature size of 15 and high accuracy (option "Slow"). The intensity was rescaled to a custom range of 0.02 to 0.2, before condensate objects with a size range from 1 to 40 were identified using the adaptive three classes Otsu algorithm with an adaptive window size of 40. Here, the "intensity" mode was used for both declumping options, while other options were left at default. Relating nuclei and condensate objects gave a new object set, nuclear condensates, which were resized by a factor of 0.5 to original size before measuring the sizes of individual condensates. Statistics were calculated and graphs were plotted using GraphPad Prism 10, using recommended settings, including for correction for multiple comparisons.

Analytical ultracentrifugation: Sedimentation velocity experiments were performed on a Beckman Coulter Optima AUC at the Canadian Center for Hydrodynamics at the University of Lethbridge. All samples were measured at 37 µM in 10 mM tris pH 8.0, 50 mM NaCl, and 1 mM TCEP. They were measured in epon-charcoal centerpieces fitted with quartz windows and measured in intensity mode at 40,000 RPM and 20°C. Data was collected at 280 nm for all samples except Ph 1397-1577 pos.SAM L1565R (EH mutant), which was measured at 296 nm, so that the absorbance was within the dynamic range of the detector. Despite the higher concentration of L1565R mutant used in the experiment, no oligomerization was detected indicating the mutation prevents all polymerization. All data were analyzed with UltraScan III version 4.0[86] and fitted with an iterative two-dimensional spectrum analysis[87] to fit the meniscus position and time- and radially-invariant noises. Diffusion-corrected integral sedimentation coefficient distributions were generated using the enhanced van Holde-Weischet analysis methods[88]. UltraScan calculated the buffer density and viscosity to be 1.000580 g/cm^3 and 1.00536 cP, respectively.

Molecular dynamics (MD) simulations and analysis: MD simulations were conducted using a coarse-grained (CG) protein model. We used the Hydropathy Scale (HPS) – Urry model[89], a recently developed single bead per amino acid CG model which has been shown to capture intrinsically disordered protein phase separation in significant agreement with *in vitro* behavior. In the HPS framework[90], the total interaction energy of the system comes from three different sources, nonbonded interactions driven by hydropathy, electrostatics, and bonded interactions between consecutive amino acids on the protein sequence,

$$U_{tot} = \sum_{i,j} \phi_{ij}^{vdw} + \sum_{i,j} \phi_{ij}^{el} + \sum_{i=1}^{N-1} k_b \left(r_{i,i+1} - r_0\right)^2, \quad (3)$$

Here the first two terms are because of nonbonded interactions whereas the last term comes from the harmonic springs connecting bonded amino acids. $k_b = 20$ kJ/Å is the spring constant for the harmonic potential and $r_0 = 3.82$ Å is the equilibrium bond length. The first term $\phi_{i,j}^{vdw}$ is the short-range van der Waals interaction between residues i and j, and is modeled using the Ashbaugh and Hatch[91] functional form given by,

$$\phi_{ij}(r) = \begin{cases} \phi_{ij}^{LJ}(r) + (1-\lambda_{ij})\epsilon, & r \leq 2^{1/6}\sigma_{ij} \\ \lambda_{ij}\phi_{ij}^{LJ}(r), & r > 2^{1/6}\sigma_{ij}, \end{cases} \quad (4)$$

Where $\phi_{ij}^{LJ}(r)$ is the standard Lennard-Jones (LJ) potential,

$$\phi_{ij}^{LJ}(r) = 4\epsilon\left[\left(\frac{\sigma_{ij}}{r}\right)^{12} - \left(\frac{\sigma_{ij}}{r}\right)^{6}\right]. \quad (5)$$

$\epsilon = 0.2$ kcal/mol is the overall energy parameter and the $\sigma_{i,j} = (\sigma_i + \sigma_j)/2$ is the distance parameter that is the average van der Waals distance between residues i and j. $\lambda_{i,j} = \mu * \frac{\lambda_i^0 + \lambda_j^0}{2} - \Delta$ where λ_i^0 is the hydropathy parameter for amino acid i which is derived from the Urry hydropathy scale[92] after it is normalized to range from 0 to 1. $\mu = 1.0$ is the scale parameter and $\Delta = 0.08$ is the shift parameter both which are derived via an optimization procedure to provide improved agreement with *in vitro* behavior of intrinsically disordered proteins. $\phi_{i,j}^{el}$ represents the contribution from the electrostatic interactions between fully charged amino acids (Lys, Arg:+1.0 and Asp, Glu:-1.0) we used the Debye-Hückel functional form,

$$\phi_{ij}^{el}(r) = \frac{q_i q_j}{4\pi D r} e^{-\kappa r} \quad (6)$$

Where q_i is the charge of residue of i and is located at the centre of the bead, D=80 (dielectric constant of water) is the dielectric constant of the medium, and κ is the inverse Debye screening length which is a proxy for the shielding effect of salt ions (1 nm^{-1} is equivalent to roughly 100 mM of salt).

The linker-SAM model was constructed by connecting the disordered linker to the SAM domain (PDB 1KW4) using MODELLER[93]. All single chain simulations were conducted for 5 μs using LAMMPS[94] Multichain simulations were conducted for 2 μs using HOOMD-Blue 2.9.3[95] SAM folded domain was treated as a rigid body using the hoomd.md.constrain.rigid function[96] All the simulations were performed at 300K. In the contact map analysis, two residues were considered in contact if the distance between them was less than 1.5 of their van der Waals arithmetic mean.

References

1. Boeynaems, S., Chong, S., Gsponer, J., Holt, L., Milovanovic, D., Mitrea, D.M., Mueller-Cajar, O., Portz, B., Reilly, J.F., Reinkemeier, C.D., et al. (2023). Phase Separation in Biology and Disease; Current Perspectives and Open Questions. J. Mol. Biol. *435*, 167971. 10.1016/j.jmb.2023.167971.

2. Mohanty, P., Kapoor, U., Sundaravadivelu Devarajan, D., Phan, T.M., Rizuan, A., and Mittal, J. (2022). Principles Governing the Phase Separation of Multidomain Proteins. Biochemistry *61*, 2443–2455. 10.1021/acs.biochem.2c00210.

3. Dong, X., and Weng, Z. (2013). The correlation between histone modifications and gene expression. Epigenomics *5*, 113–116.

4. Dignon, G.L., Best, R.B., and Mittal, J. (2020). Biomolecular Phase Separation: From Molecular Driving Forces to Macroscopic Properties. Annu. Rev. Phys. Chem. *71*, 53–75. 10.1146/annurev-physchem-071819-113553.

5. Dixon, J.R. (2015). Chromatin architecture reorganization during stem cell differentiation. Nature *518*, 331–336.

6. Dai, Y., You, L., and Chilkoti, A. (2023). Engineering synthetic biomolecular condensates. Nat. Rev. Bioeng. *1*, 466–480. 10.1038/s44222-023-00052-6.

7. Bowman, G.D., and Poirier, M.G. (2015). Post-Translational Modifications of Histones That Influence Nucleosome Dynamics. Chem Rev *115*, 2274–2295.

8. Dong, X., and Weng, Z. (2013). The correlation between histone modifications and gene expression. Epigenomics *5*, 113–116. 10.2217/epi.13.13.

9. Boltsis, I., Grosveld, F., Giraud, G., and Kolovos, P. (2021). Chromatin Conformation in Development and Disease. Front Cell Dev Biol *9*.

10. Dixon, J.R., Jung, I., Selvaraj, S., Shen, Y., Antosiewicz-Bourget, J.E., Lee, A.Y., Ye, Z., Kim, A., Rajagopal, N., Xie, W., et al. (2015). Chromatin architecture reorganization during stem cell differentiation. Nature *518*, 331–336. 10.1038/nature14222.

11. Deng, S., Feng, Y., and Pauklin, S. (2022). 3D chromatin architecture and transcription regulation in cancer. J Hematol Amp Oncol *15*.

12. Bowman, G.D., and Poirier, M.G. (2015). Post-Translational Modifications of Histones That Influence Nucleosome Dynamics. Chem. Rev. *115*, 2274–2295. 10.1021/cr500350x.

13. Robinson, A.K. (2012). Human polyhomeotic homolog 3 (PHC3) sterile alpha motif (SAM) linker allows open-ended polymerization of PHC3 SAM. Biochemistry *51*, 5379–5386.

14. Boltsis, I., Grosveld, F., Giraud, G., and Kolovos, P. (2021). Chromatin Conformation in Development and Disease. Front. Cell Dev. Biol. *9*. 10.3389/fcell.2021.723859.

15. Croce, L., and Helin, K. (2013). Transcriptional regulation by Polycomb group proteins. Nat Struct Mol Biol *20*, 1147–1155.

16. Deng, S., Feng, Y., and Pauklin, S. (2022). 3D chromatin architecture and transcription regulation in cancer. J. Hematol. Amp Oncol. *15*. 10.1186/s13045-022-01271-x.

17. Entrevan, M., Schuettengruber, B., and Cavalli, G. (2016). Regulation of Genome Architecture and Function by Polycomb Proteins. Trends Cell Biol *26*, 511–525.

18. Robinson, A.K., Leal, B.Z., Nanyes, D.R., Kaur, Y., Ilangovan, U., Schirf, V., Hinck, A.P., Demeler, B., and Kim, C.A. (2012). Human polyhomeotic homolog 3 (PHC3) sterile alpha motif (SAM) linker allows open-ended polymerization of PHC3 SAM. Biochemistry *51*, 5379–5386. 10.1021/bi3004318.

19. Kassis, J.A., Kennison, J.A., and Tamkun, J.W. (2017). Polycomb and trithorax group genes in drosophila. Genetics *206*, 1699–1725.

20. Di Croce, L., and Helin, K. (2013). Transcriptional regulation by Polycomb group proteins. Nat. Struct. Mol. Biol. *20*, 1147–1155. 10.1038/nsmb.2669.

21. Loubiere, V., Martinez, A.M., and Cavalli, G. (2019). Cell Fate and Developmental Regulation Dynamics by Polycomb Proteins and 3D Genome Architecture. BioEssays *41*, 1800222.

22. Entrevan, M., Schuettengruber, B., and Cavalli, G. (2016). Regulation of Genome Architecture and Function by Polycomb Proteins. Trends Cell Biol. *26*, 511–525. 10.1016/j.tcb.2016.04.009.

23. Saurin, A.J. (1998). The human polycomb group complex associates with pericentromeric heterochromatin to form a novel nuclear domain. J Cell Biol *142*, 887–898.

24. Kassis, J.A., Kennison, J.A., and Tamkun, J.W. (2017). Polycomb and trithorax group genes in drosophila. Genetics *206*, 1699–1725. 10.1534/genetics.115.185116.

25. Cheutin, T., and Cavalli, G. (2012). Progressive polycomb assembly on H3K27me3 compartments generates Polycomb bodies with developmentally regulated motion. PLoS Genet *8*, 1002465.

26. Loubiere, V., Martinez, A.M., and Cavalli, G. (2019). Cell Fate and Developmental Regulation Dynamics by Polycomb Proteins and 3D Genome Architecture. BioEssays *41*, 1800222. 10.1002/bies.201800222.

27. Isono, K. (2013). SAM domain polymerization links subnuclear clustering of PRC1 to gene silencing. Dev Cell *26*, 565–577.

28. Saurin, A.J., Shiels, C., Williamson, J., Satijn, D.P.E., Otte, A.P., Sheer, D., and Freemont, P.S. (1998). The human polycomb group complex associates with pericentromeric

heterochromatin to form a novel nuclear domain. J. Cell Biol. *142*, 887–898. 10.1083/jcb.142.4.887.

29. Wani, A.H. (2016). Chromatin topology is coupled to Polycomb group protein subnuclear organization. Nat Commun *7*.

30. Cheutin, T., and Cavalli, G. (2012). Progressive polycomb assembly on H3K27me3 compartments generates Polycomb bodies with developmentally regulated motion. PLoS Genet. *8*, e1002465. 10.1371/journal.pgen.1002465.

31. Tatavosian, R. (2019). Nuclear condensates of the Polycomb protein chromobox 2 (CBX2) assemble through phase separation. J Biol Chem *294*, 1451–1463.

32. Isono, K., Endo, T.A., Ku, M., Yamada, D., Suzuki, R., Sharif, J., Ishikura, T., Toyoda, T., Bernstein, B.E., and Koseki, H. (2013). SAM domain polymerization links subnuclear clustering of PRC1 to gene silencing. Dev. Cell *26*, 565–577. 10.1016/j.devcel.2013.08.016.

33. Eeftens, J.M., Kapoor, M., Michieletto, D., and Brangwynne, C.P. (2021). Polycomb condensates can promote epigenetic marks but are not required for sustained chromatin compaction. Nat Commun *12*.

34. Wani, A.H., Boettiger, A.N., Schorderet, P., Ergun, A., Munger, C., Sadreyev, R.I., Zhuang, X., Kingston, R.E., and Francis, N.J. (2016). Chromatin topology is coupled to Polycomb group protein subnuclear organization. Nat. Commun. *7*. 10.1038/ncomms10291.

35. Robinson, A.K. (2012). The growth-suppressive function of the polycomb group protein polyhomeotic is mediated by polymerization of its sterile alpha motif (SAM) domain. J Biol Chem *287*, 8702–8713.

36. Tatavosian, R., Kent, S., Brown, K., Yao, T., Duc, H.N., Huynh, T.N., Zhen, C.Y., Ma, B., Wang, H., and Ren, X. (2019). Nuclear condensates of the Polycomb protein chromobox 2 (CBX2) assemble through phase separation. J. Biol. Chem. *294*, 1451–1463. 10.1074/jbc.RA118.006620.

37. Gambetta, M.C., and Müller, J. (2014). O-GlcNAcylation Prevents Aggregation of the Polycomb Group Repressor Polyhomeotic. Dev Cell *31*, 629–639.

38. Eeftens, J.M., Kapoor, M., Michieletto, D., and Brangwynne, C.P. (2021). Polycomb condensates can promote epigenetic marks but are not required for sustained chromatin compaction. Nat. Commun. *12*. 10.1038/s41467-021-26147-5.

39. Cheutin, T., and Cavalli, G. (2018). Loss of PRC1 induces higher-order opening of Hox loci independently of transcription during Drosophila embryogenesis. Nat Commun *9*.

40. Robinson, A.K., Leal, B.Z., Chadwell, L. V., Wang, R., Ilangovan, U., Kaur, Y., Junco, S.E., Schirf, V., Osmulski, P.A., Gaczynska, M., et al. (2012). The growth-suppressive function of the polycomb group protein polyhomeotic is mediated by polymerization of its sterile alpha motif (SAM) domain. J. Biol. Chem. *287*, 8702–8713. 10.1074/jbc.M111.336115.

41. Loubiere, V., Papadopoulos, G.L., Szabo, Q., Martinez, A.M., and Cavalli, G. (2020). Widespread activation of developmental gene expression characterized by PRC1-dependent chromatin looping. Sci Adv *6*, 4001.

42. Gambetta, M.C., and Müller, J. (2014). O-GlcNAcylation Prevents Aggregation of the Polycomb Group Repressor Polyhomeotic. Dev. Cell *31*, 629–639. 10.1016/j.devcel.2014.10.020.

43. Saurin, A.J. (1998). The Human Polycomb Group Complex Associates with Pericentromeric Heterochromatin to Form a Novel Nuclear Domain. J Cell Biol *142*, 887–898.

44. Cheutin, T., and Cavalli, G. (2018). Loss of PRC1 induces higher-order opening of Hox loci independently of transcription during Drosophila embryogenesis. Nat. Commun. *9*. 10.1038/s41467-018-05945-4.

45. Hernández-Muñoz, I., Taghavi, P., Kuijl, C., Neefjes, J., and Lohuizen, M. (2005). Association of BMI1 with Polycomb Bodies Is Dynamic and Requires PRC2/EZH2 and the Maintenance DNA Methyltransferase DNMT1. Mol Cell Biol *25*, 11047–11058.

46. Loubiere, V., Papadopoulos, G.L., Szabo, Q., Martinez, A.M., and Cavalli, G. (2020). Widespread activation of developmental gene expression characterized by PRC1-dependent chromatin looping. Sci. Adv. *6*, eaax4001. 10.1126/sciadv.aax4001.

47. Bantignies, F. (2011). Polycomb-Dependent Regulatory Contacts between Distant Hox Loci in Drosophila. Cell *144*, 214–226.

48. Cho, W.-K., Spille, J.-H., Hecht, M., Lee, C., Li, C., Grube, V., and Cisse, I.I. (2018). Mediator and RNA polymerase II clusters associate in transcription-dependent condensates. Science *361*, 412–415. 10.1126/science.aar4199.

49. Kim, C.A., Gingery, M., Pilpa, R.M., and Bowie, J.U. (2002). The SAM domain of polyhomeotic forms a helical polymer. Nat Struct Biol *9*, 453–457.

50. Saurin, A.J., Shiels, C., Williamson, J., Satijn, D.P.E., Otte, A.P., Sheer, D., and Freemont, P.S. (1998). The Human Polycomb Group Complex Associates with Pericentromeric Heterochromatin to Form a Novel Nuclear Domain. J. Cell Biol. *142*, 887–898. 10.1083/jcb.142.4.887.

51. Plys, A.J. (2019). Phase separation of Polycomb-repressive complex 1 is governed by a charged disordered region of CBX2. Genes Dev *33*, 799–813.

52. Hernández-Muñoz, I., Taghavi, P., Kuijl, C., Neefjes, J., and Van Lohuizen, M. (2005). Association of BMI1 with Polycomb Bodies Is Dynamic and Requires PRC2/EZH2 and the Maintenance DNA Methyltransferase DNMT1. Mol. Cell. Biol. *25*, 11047–11058. 10.1128/mcb.25.24.11047-11058.2005.

53. Kent, S. (2020). Phase-Separated Transcriptional Condensates Accelerate Target-Search Process Revealed by Live-Cell Single-Molecule Imaging. Cell Rep *33*, 108248.

54. Bantignies, F., Roure, V., Comet, I., Leblanc, B., Schuettengruber, B., Bonnet, J., Tixier, V., Mas, A., and Cavalli, G. (2011). Polycomb-Dependent Regulatory Contacts between Distant Hox Loci in Drosophila. Cell *144*, 214–226. 10.1016/j.cell.2010.12.026.

55. Baumann, C., Zhang, X., and Fuente, R. (2020). Loss of CBX2 induces genome instability and senescence-associated chromosomal rearrangements. J Cell Biol *219*.

56. Kundu, S., Ji, F., Sunwoo, H., Jain, G., Lee, J.T., Sadreyev, R.I., Dekker, J., and Kingston, R.E. (2017). Polycomb Repressive Complex 1 Generates Discrete Compacted Domains that Change during Differentiation. Mol. Cell *65*, 432-446.e5. 10.1016/j.molcel.2017.01.009.

57. Del Gaudio, N. (2022). CBX2 shapes chromatin accessibility promoting AML via p38 MAPK signaling pathway. Mol Cancer *21*.

58. Kim, C.A., Gingery, M., Pilpa, R.M., and Bowie, J.U. (2002). The SAM domain of polyhomeotic forms a helical polymer. Nat. Struct. Biol. *9*, 453–457. 10.1038/nsb802.

59. Kapur, I., Boulier, E.L., and Francis, N.J. (2022). Regulation of Polyhomeotic Condensates by Intrinsically Disordered Sequences That Affect Chromatin Binding. Epigenomes *6*, 40.

60. Plys, A.J., Davis, C.P., Kim, J., Rizki, G., Keenen, M.M., Marr, S.K., and Kingston, R.E. (2019). Phase separation of Polycomb-repressive complex 1 is governed by a charged disordered region of CBX2. Genes Dev. *33*, 799–813. 10.1101/gad.326488.119.

61. Gray, F. (2016). BMI1 regulates PRC1 architecture and activity through homo- and hetero-oligomerization. Nat Commun *7*.

62. Tatavosian, R., Kent, S., Brown, K., Yao, T., Duc, H.N., Huynh, T.N., Zhen, C.Y., Ma, B., Wang, H., and Ren, X. (2019). Nuclear condensates of the Polycomb protein chromobox 2 (CBX2) assemble through phase separation. J. Biol. Chem. *294*, 1451–1463. 10.1074/jbc.RA118.006620.

63. Wang, R. (2011). Identification of nucleic acid binding residues in the FCS domain of the polycomb group protein polyhomeotic. Biochemistry *50*, 4998–5007.

64. Brown, K., Chew, P.Y., Ingersoll, S., Espinosa, J.R., Aguirre, A., Espinoza, A., Wen, J., Astatike, K., Kutateladze, T.G., Collepardo-Guevara, R., et al. (2023). Principles of assembly and regulation of condensates of Polycomb repressive complex 1 through phase separation. Cell Rep. *42*, 113136. 10.1016/j.celrep.2023.113136.

65. Seif, E. (2020). Phase separation by the polyhomeotic sterile alpha motif compartmentalizes Polycomb Group proteins and enhances their activity. Nat Commun *11*, 5609.

66. Kent, S., Brown, K., Yang, C.-H., Alsaihati, N., Tian, C., Wang, H., and Ren, X. (2020). Phase-Separated Transcriptional Condensates Accelerate Target-Search Process Revealed by Live-Cell Single-Molecule Imaging. Cell Rep. *33*, 108248. 10.1016/j.celrep.2020.108248.

67. Loubiere, V. (2016). Coordinate redeployment of PRC1 proteins suppresses tumor formation during Drosophila development. Nat Genet *48*, 1436–1442.

68. Baumann, C., Zhang, X., and De La Fuente, R. (2020). Loss of CBX2 induces genome instability and senescence-associated chromosomal rearrangements. J. Cell Biol. *219*. 10.1083/jcb.201910149.

69. Berg, S., Kutra, D., Kroeger, T., Straehle, C.N., Kausler, B.X., Haubold, C., Schiegg, M., Ales, J., Beier, T., Rudy, M., et al. (2019). ilastik: interactive machine learning for (bio)image analysis. Nat. Methods. 10.1038/s41592-019-0582-9.

70. Del Gaudio, N., Di Costanzo, A., Liu, N.Q., Conte, L., Dell'Aversana, C., Bove, G., Benedetti, R., Montella, L., Ciardiello, F., Carafa, V., et al. (2022). CBX2 shapes chromatin accessibility promoting AML via p38 MAPK signaling pathway. Mol. Cancer *21*. 10.1186/s12943-022-01603-y.

71. Schindelin, J., Arganda-Carreras, I., Frise, E., Kaynig, V., Longair, M., Pietzsch, T., Preibisch, S., Rueden, C., Saalfeld, S., Schmid, B., et al. (2012). Fiji: an open-source platform for biological-image analysis. Nat. Methods *9*, 676–682. 10.1038/nmeth.2019.

72. Kapur, I., Boulier, E.L., and Francis, N.J. (2022). Regulation of Polyhomeotic Condensates by Intrinsically Disordered Sequences That Affect Chromatin Binding. Epigenomes *6*, 40. 10.3390/epigenomes6040040.

73. Gray, F., Cho, H.J., Shukla, S., He, S., Harris, A., Boytsov, B., Jaremko, A., Jaremko, M., Demeler, B., Lawlor, E.R., et al. (2016). BMI1 regulates PRC1 architecture and activity through homo- and hetero-oligomerization. Nat. Commun. *7*. 10.1038/ncomms13343.

74. Wang, R., Ilangovan, U., Leal, B.Z., Robinson, A.K., Amann, B.T., Tong, C. V., Berg, J.M., Hinck, A.P., and Kim, C.A. (2011). Identification of nucleic acid binding residues in the FCS domain of the polycomb group protein polyhomeotic. Biochemistry *50*, 4998–5007. 10.1021/bi101487s.

75. Seif, E., Kang, J.J., Sasseville, C., Senkovich, O., Kaltashov, A., Boulier, E.L., Kapur, I., Kim, C.A., and Francis, N.J. (2020). Phase separation by the polyhomeotic sterile alpha motif compartmentalizes Polycomb Group proteins and enhances their activity. Nat. Commun. *11*, 5609. 10.1038/s41467-020-19435-z.

76. Phan, T.M., Kim, Y.C., Debelouchina, G.T., and Mittal, J. (2023). Interplay between charge distribution and DNA in shaping HP1 paralog phase separation and localization. 10.7554/elife.90820.1.

77. Regy, R.M., Thompson, J., Kim, Y.C., and Mittal, J. (2021). Improved coarse-grained model for studying sequence dependent phase separation of disordered proteins. Protein Sci *30*, 1371–1379.

78. Dignon, G.L., Zheng, W., Best, R.B., Kim, Y.C., and Mittal, J. (2018). Relation between single-molecule properties and phase behavior of intrinsically disordered proteins. Proc. Natl. Acad. Sci. *115*, 9929–9934. 10.1073/pnas.1804177115.

79. Loubiere, V., Delest, A., Thomas, A., Bonev, B., Schuettengruber, B., Sati, S., Martinez, A.M., and Cavalli, G. (2016). Coordinate redeployment of PRC1 proteins suppresses tumor formation during Drosophila development. Nat. Genet. *48*, 1436–1442. 10.1038/ng.3671.

80. Daniel Bsteh, Hagar F. Moussa, Georg Michlits, Ramesh Yelagandula, Jingkui Wang, Ulrich Elling, and Oliver Bell (2021). Loss of Cohesin regulator PDS5A reveals repressive role of Polycomb loops. bioRxiv, 2021.12.15.472841. 10.1101/2021.12.15.472841.

81. Kundu, S. (2017). Polycomb Repressive Complex 1 Generates Discrete Compacted Domains that Change during Differentiation. Mol Cell *65*, 432-446 5.

82. Gibson, B.A., Blaukopf, C., Lou, T., Chen, L., Doolittle, L.K., Finkelstein, I., Narlikar, G.J., Gerlich, D.W., and Rosen, M.K. (2023). In diverse conditions, intrinsic chromatin condensates have liquid-like material properties. Proc. Natl. Acad. Sci. U. S. A. *120*, e2218085120. 10.1073/pnas.2218085120.

83. Schindelin, J., Arganda-Carreras, I., Frise, E., Kaynig, V., Longair, M., Pietzsch, T., Preibisch, S., Rueden, C., Saalfeld, S., Schmid, B., et al. (2012). Fiji: an open-source platform for biological-image analysis. Nat. Methods *9*, 676–682. 10.1038/nmeth.2019.

84. Stirling, D.R., Swain-Bowden, M.J., Lucas, A.M., Carpenter, A.E., Cimini, B.A., and Goodman, A. (2021). CellProfiler 4: improvements in speed, utility and usability. BMC Bioinformatics *22*, 433. 10.1186/s12859-021-04344-9.

85. Berg, S., Kutra, D., Kroeger, T., Straehle, C.N., Kausler, B.X., Haubold, C., Schiegg, M., Ales, J., Beier, T., Rudy, M., et al. (2019). ilastik: interactive machine learning for (bio)image analysis. Nat. Methods. 10.1038/s41592-019-0582-9.

86. Demeler, B., and Gorbet, G.E. (2016). Analytical Ultracentrifugation Data Analysis with UltraScan-III. In Analytical Ultracentrifugation: Instrumentation, Software, and Applications, S. Uchiyama, F. Arisaka, W. F. Stafford, and T. Laue, eds. (Springer Japan), pp. 119–143. 10.1007/978-4-431-55985-6_8.

87. Brookes, E., Cao, W., and Demeler, B. (2010). A two-dimensional spectrum analysis for sedimentation velocity experiments of mixtures with heterogeneity in molecular weight and shape. Eur. Biophys. J. EBJ *39*, 405–414. 10.1007/s00249-009-0413-5.

88. Demeler, B., and van Holde, K.E. (2004). Sedimentation velocity analysis of highly heterogeneous systems. Anal. Biochem. *335*, 279–288. 10.1016/j.ab.2004.08.039.

89. Regy, R.M., Thompson, J., Kim, Y.C., and Mittal, J. (2021). Improved coarse-grained model for studying sequence dependent phase separation of disordered proteins. Protein Sci. *30*, 1371–1379. 10.1002/pro.4094.

90. Dignon, G.L., Zheng, W., Kim, Y.C., Best, R.B., and Mittal, J. (2018). Sequence determinants of protein phase behavior from a coarse-grained model. PLOS Comput. Biol. *14*, e1005941. 10.1371/journal.pcbi.1005941.

91. Ashbaugh, H.S., and Hatch, H.W. (2008). Natively Unfolded Protein Stability as a Coil-to-Globule Transition in Charge/Hydropathy Space. J. Am. Chem. Soc. *130*, 9536–9542. 10.1021/ja802124e.

92. Urry, D.W., Gowda, D.C., Parker, T.M., Luan, C.H., Reid, M.C., Harris, C.M., Pattanaik, A., and Harris, R.D. (1992). Hydrophobicity scale for proteins based on inverse temperature transitions. Biopolymers *32*, 1243–1250. 10.1002/bip.360320913.

93. Eswar, N., Webb, B., Marti-Renom, M.A., Madhusudhan, M.S., Eramian, D., Shen, M., Pieper, U., and Sali, A. (2006). Comparative Protein Structure Modeling Using Modeller. Curr. Protoc. Bioinforma. *15*, 5.6.1-5.6.30. 10.1002/0471250953.bi0506s15.

94. Plimpton, S. (1995). Fast Parallel Algorithms for Short-Range Molecular Dynamics. J. Comput. Phys. *117*, 1–19. 10.1006/jcph.1995.1039.

95. Anderson, J.A., Glaser, J., and Glotzer, S.C. (2020). HOOMD-blue: A Python package for high-performance molecular dynamics and hard particle Monte Carlo simulations. Comput. Mater. Sci. *173*, 109363. 10.1016/j.commatsci.2019.109363.

96. Nguyen, T.D., Phillips, C.L., Anderson, J.A., and Glotzer, S.C. (2011). Rigid body constraints realized in massively-parallel molecular dynamics on graphics processing units. Comput. Phys. Commun. *182*, 2307–2313. 10.1016/j.cpc.2011.06.005.

Supplementary Materials

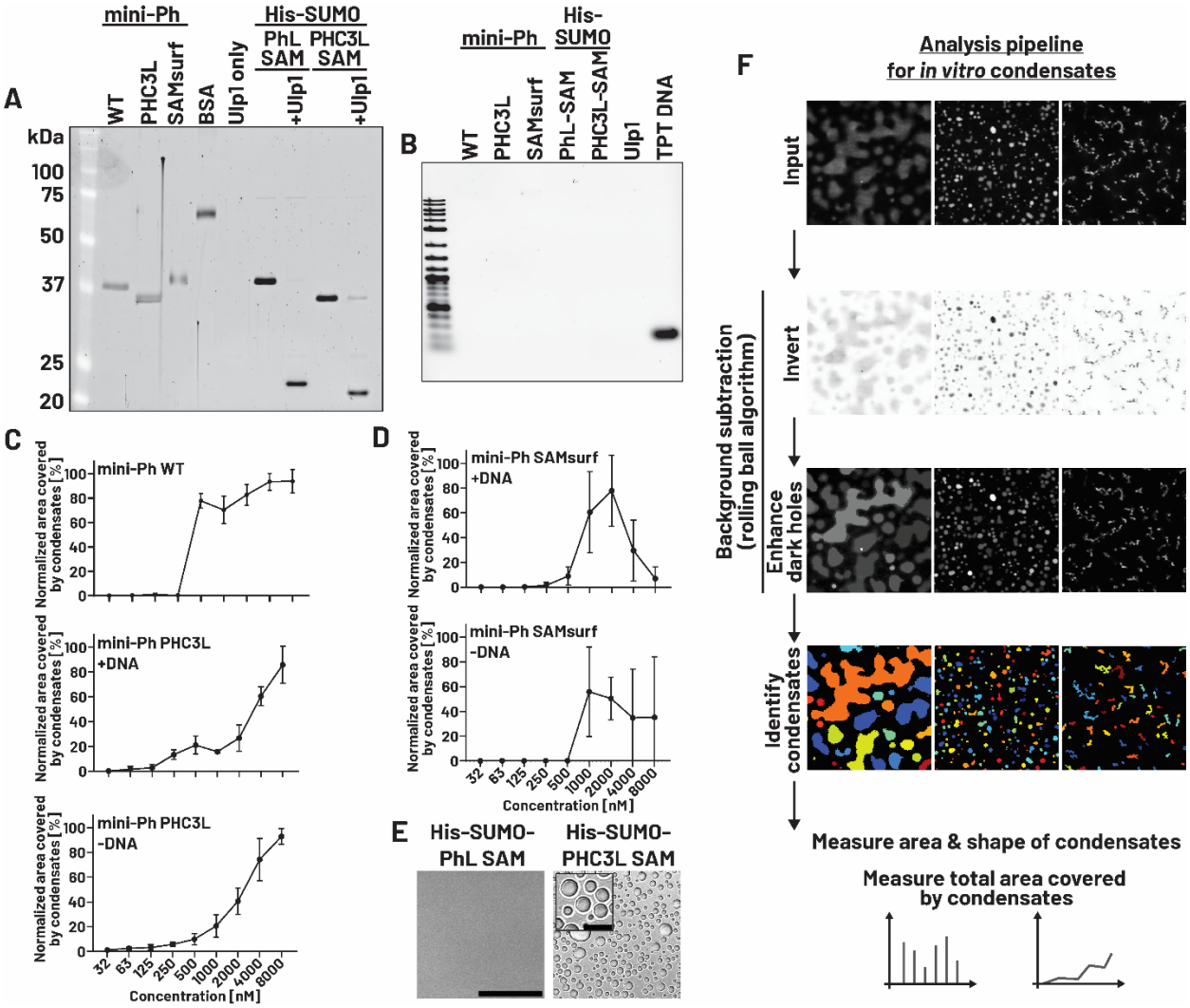

Supplementary Figure 1: A. SDS-PAGE of proteins used in *in vitro* assays. SUMO protease Ulp1 cleaves the His-SUMO tag from linker-SAM proteins resulting in size shift. B. DNA agarose gel of proteins in A after proteinase K treatment indicates absence of DNA contaminations in protein preps. 156 bp TPT DNA (50 ng) used for *in vitro* phase separation assays was loaded as a reference. C+D. Quantification of total area covered by condensates in *in vitro* phase separation assays. These informed titration summaries (qualitative phase diagrams) shown in Figures 1C and 4C. E. Phase contrast images of HisSUMO-PhL-SAM and HisSUMO-PHC3L-SAM without cleavage of SUMO tag with Ulp1 (compare Figure 1J). Scale bar: 50 µm and 10 µm for inlay. F. Overview of analysis pipeline for *in vitro* condensates. All indicated steps were performed in CellProfiler 4.2.5[84].

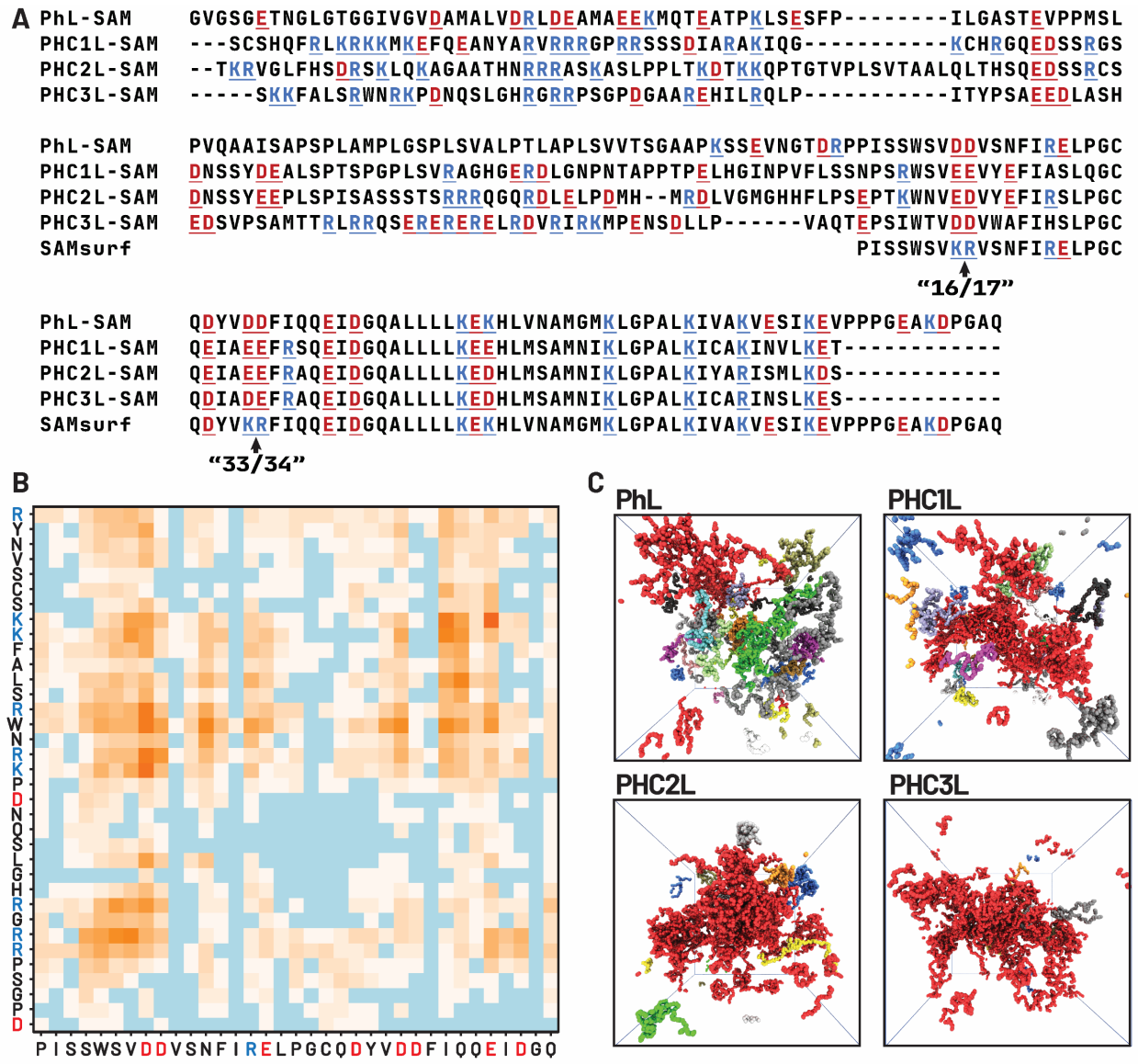

Supplementary Figure 2: A. Sequence alignments of linker-SAM sequences from Ph and PHCs, and alignment of SAMsurf mutant with acidic-to-basic mutations indicated. B. Zoom on contact map region with increased PHC3L-SAM contact frequency in Figure 2C from single chain simulations. Individual residues are indicated (PHC3L residues on y axis, SAM residues on x axis) with basic residues (K and R) in blue and acidic residues (D and E) in red. Note that simulations were conducted on PHC3L-SAM chains with additional N-terminal residues (RYNVSC) as compared with PhL-SAM. C. Snapshots from simulations corresponding to clustering data (Figure 2J), where chains belonging to the largest cluster are colored red.

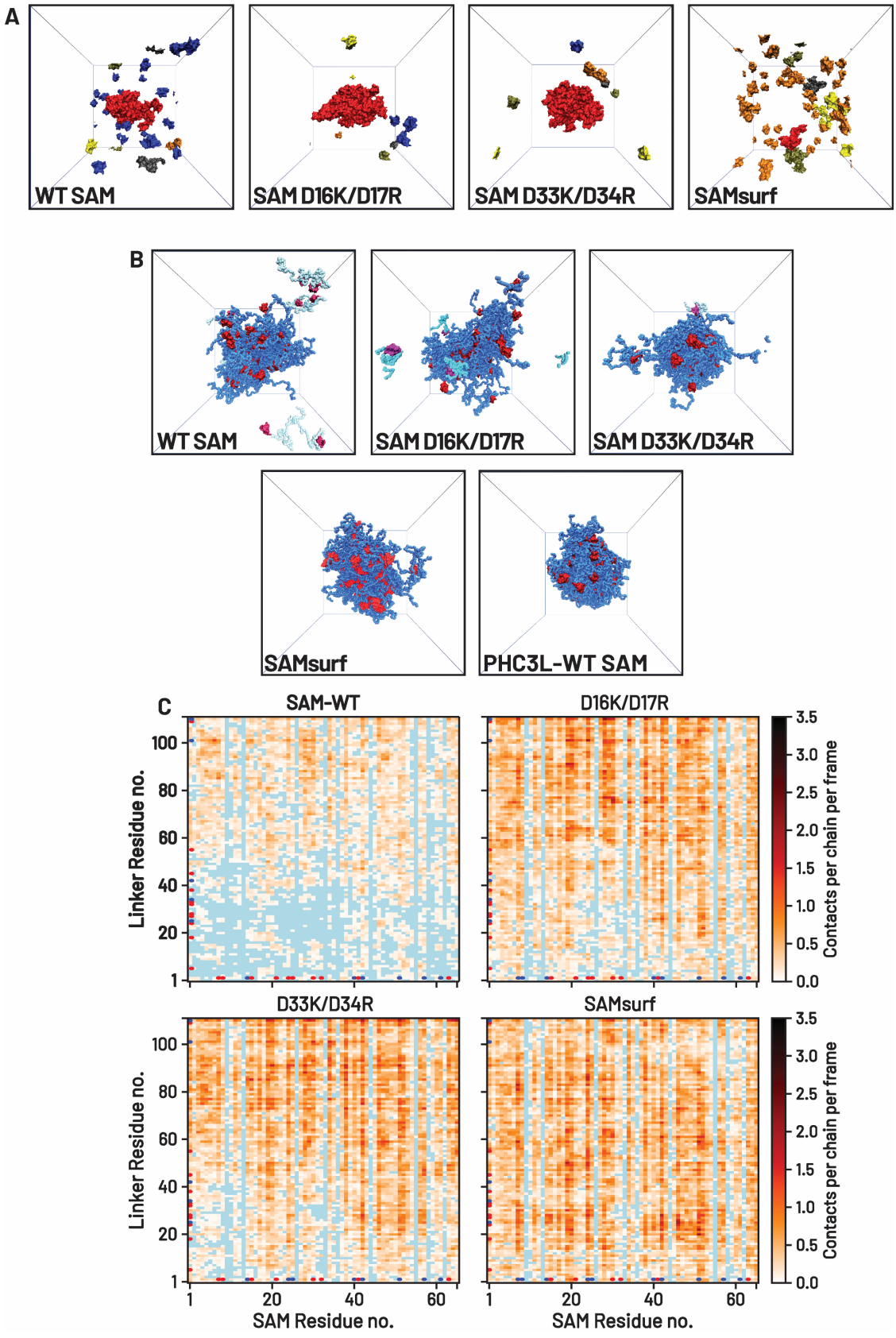

Supplementary Figure 3: A. Snapshots from multi chain simulations corresponding to SAM clustering data (Figure 3D), where chains belonging to the largest cluster are colored red. B. Snapshots from multi chain simulations of PhL with WT SAM (same as Figure 2D) or SAM surface mutants as well as PHC3L with WT SAM (same as Figure 2E). Linkers that are not part of the largest cluster are colored light blue. C. Zoom on intermolecular contact map region with linker-SAM residues in Figure 3E-H from multichain simulations. Basic residues (K and R) are indicated with blue dots on the axes, acidic residues (D and E) in red.

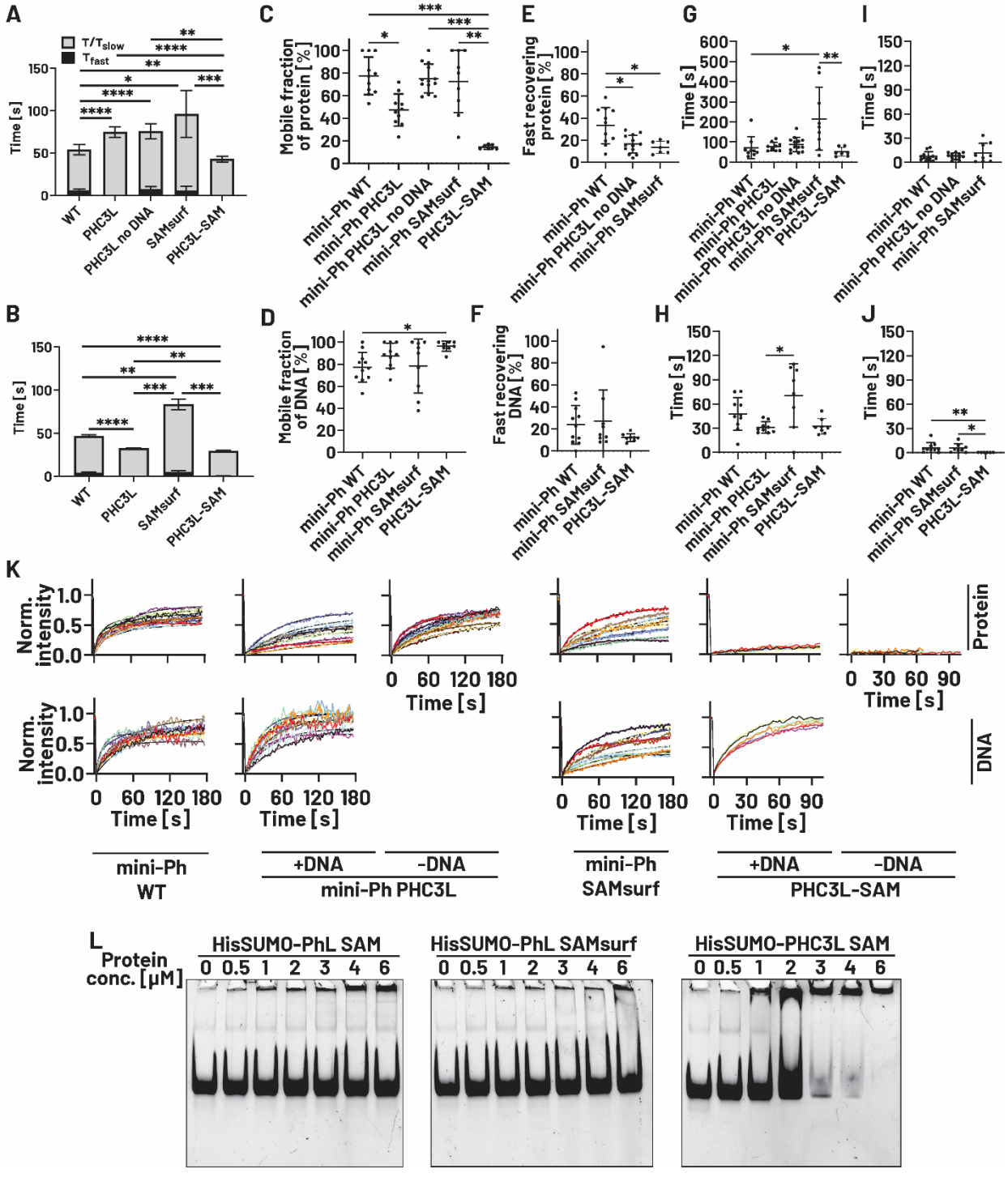

Supplementary Figure 4: A,B. τ (τ for single-exponential fit, τ_{slow} and τ_{fast} for double-exponential fit) of protein (A) and DNA (B) recovery were affected by changes in linker interactions. The parameters were obtained from the combined fits in Figure 5C with error bars representing standard deviations. τ and τ_{slow}, respectively, were compared using Dunnett's T3 test for multiple comparison. C-J. Analysis of fit parameters from individual traces in K with mean and standard deviations as error bars. C,D. Mobile protein fractions (C) and DNA fractions (D). E,F. Fast recovering protein fractions (E) and DNA fractions (F). G,H. τ (for single-exponential fit) and τ_{slow} (for double-exponential fit) of protein recovery (G) and DNA recovery (H). I+J. τ_{fast} of protein (I) and DNA (J) recovery. (for A-J *: $p<0.01$, **: $p<0.01$, ***: $p<0.001$ ****: $p<0.0001$). K. FRAP traces from individual experiments. L. Electrophoretic mobility shift assay of His-SUMO linker-SAM constructs (without Ulp1 cleavage) with 156 bp TPT DNA demonstrates DNA binding by the PHC3L but not by PhL, SAM or SAMsurf.

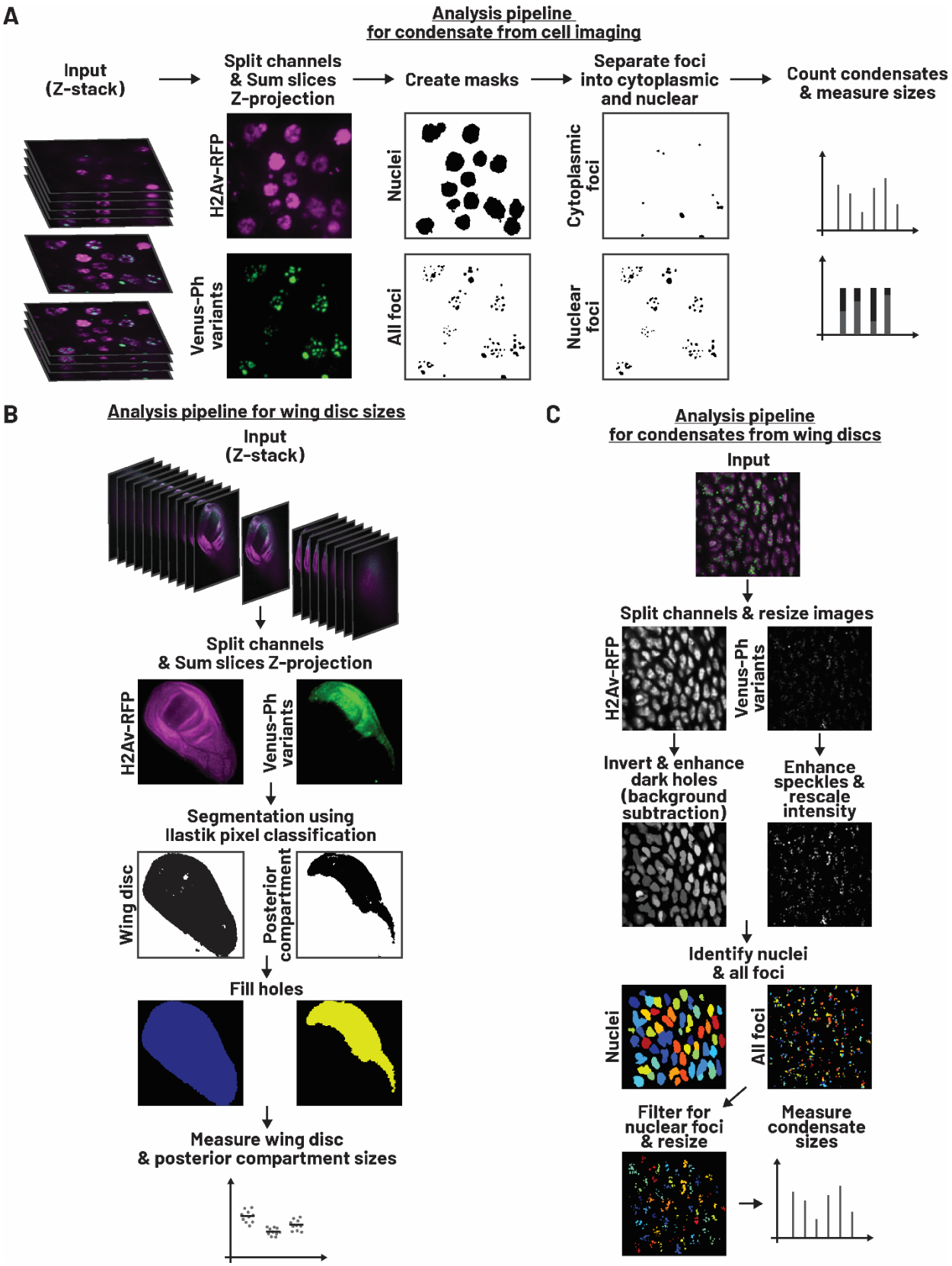

Supplementary Figure 5: A. Analysis pipeline for condensates in cultured Kc-167 cells. Indicated steps were performed in ImageJ. Quantification of condensates per cell for mini-Ph variants (Figure 6B) was conducted in CellProfiler[84] with the masks obtained from ImageJ. B. Analysis pipeline for wing discs. CellProfiler was used to split channels and Z-projections were generated with a custom ImageJ script (like in A). A simple segmentation output was obtained from Ilastik[85] by training a pixel classifier. Filling of holes in the segmentation masks and measurements of mask sizes was done in CellProfiler. C. Analysis pipeline for condensates in wing discs. All indicated steps were performed in CellProfiler.

Table 1: Protein sequences of linker, SAM and mini-Ph variants

Name	**Sequence**
PhSAM WT	PPISSWSVDDVSNFIRELPGCQDYVDDFIQQEIDGQALLLLKEKHLVNAMGMKLGPAL KIVAKVESIKEVPPPGEAKDPGAQ
SAM D16K/D17R	PPISSWSVKRVSNFIRELPGCQDYVDDFIQQEIDGQALLLLKEKHLVNAMGMKLGPAL KIVAKVESIKEVPPPGEAKDPGAQ
SAM D33K/D34R	PPISSWSVDDVSNFIRELPGCQDYVKRFIQQEIDGQALLLLKEKHLVNAMGMKLGPAL KIVAKVESIKEVPPPGEAKDPGAQ
SAMsurf	PPISSWSVKRVSNFIRELPGCQDYVKRFIQQEIDGQALLLLKEKHLVNAMGMKLGPAL KIVAKVESIKEVPPPGEAKDPGAQ
SAMsurf EH	PPISSWSVKRVSNFIRELPGCQDYVKRFIQQEIDGQALLLLKEKHLVNAMGMKLGPAR KIVAKVESIKEVPPPGEAKDPGAQ
PhL	GVGSGETNGLGTGGIVGVDAMALVDRLDEAMAEEKMQTEATPKLSESFPILGASTEVP PMSLPVQAAISAPSPLAMPLGSPLSVALPTLAPLSVVTSGAAPKSSEVNGTDR
PHC1L	SCSHQFRLKRKKMKEFQEANYARVRRRGPRRSSSDIARAKIQGKCHRGQEDSSRGSD NSSYDEALSPTSPGPLSVRAGHGERDLGNPNTAPPTPELHGINPVFLS
PHC2L	TKRVGLFHSDRSKLQKAGAATHNRRRASKASLPPLTKDTKKQPTGTVPLSVTAALQL THSQEDSSRCSDNSSYEEPLSPISASSSTSRRRQGQRDLELPDMHMRDLVGMGHHFLPS
PHC3L (experiment)	SKKFALSRWNRKPDNQSLGHRGRRPSGPDGAAREHILRQLPITYPSAEEDLASHEDSVP SAMTTRLRRQSERERERELRDVRIRKMPENSDLLPVAQ
PHC3L (simulation)	RYNVSCSKKFALSRWNRKPDNQSLGHRGRRPSGPDGAAREHILRQLPITYPSAEEDLA SHEDSVPSAMTTRLRRQSERERERELRDVRIRKMPENSDLLPVAQ
Mini-Ph WT	MDYKDDDDKGSDYKDDDDKGSHRYTSLYKKAGSEFHVRGRSATRNMIKPNVLTHVI DGFIIQEANEPFPVTRQRYADKDVSDEPPKKKATMQEDIKLSGIASAPGSDMVACEQCG KMEHKAKLKRKRYCSPGCSRQAKNGIGGVGSGETNGLGTGGIVGVDAMALVDRLDE AMAEEKMQTEATPKLSESFPILGASTEVPPMSLPVQAAISAPSPLAMPLGSPLSVALPTL APLSVVTSGAAPKSSEVNGTDRPPISSWSVDDVSNFIRELPGCQDYVDDFIQQEIDGQA LLLLKEKHLVNAMGMKLGPALKIVAKVESIKEVPPPGEAKDPGAQ
Mini-Ph PHC3L	MDYKDDDDKPGPKKKRKVRNSKDLPKAMIKPNVLTHVIDGFIIQEANEPFPVTRQRYA DKDVSDEPPKKKATMQEDIKLSGIASAPGSDMVACEQCGKMEHKAKLKRKRYCSPGC SRQAKNGIGSKKFALSRWNRKPDNQSLGHRGRRPSGPDGAAREHILRQLPITYPSAEE DLASHEDSVPSAMTTRLRRQSERERERELRDVRIRKMPENSDLLPVAQPPISSWSVDD VSNFIRELPGCQDYVDDFIQQEIDGQALLLLKEKHLVNAMGMKLGPALKIVAKVESIKE VPPPGEAKDPGAQ
Mini-Ph SAMsurf	MDYKDDDDKGSDYKDDDDKGSHRYTSLYKKAGSEFHVRGRSATRNMIKPNVLTHVI DGFIIQEANEPFPVTRQRYADKDVSDEPPKKKATMQEDIKLSGIASAPGSDMVACEQCG KMEHKAKLKRKRYCSPGCSRQAKNGIGGVGSGETNGLGTGGIVGVDAMALVDRLDE AMAEEKMQTEATPKLSESFPILGASTEVPPMSLPVQAAISAPSPLAMPLGSPLSVALPTL APLSVVTSGAAPKSSEVNGTDRPPISSWSVKRVSNFIRELPGCQDYVKRFIQQEIDGQA LLLLKEKHLVNAMGMKLGPALKIVAKVESIKEVPPPGEAKDPGAQ